ORNL/TM-2023/3201

Photonuclear Physics in SCALE

Jesse Brown
Cihangir Celik
Thomas Evans
BK Jeon
Robert Lefebvre [1]
Jordan McDonnell
Katherine Royston
Dorothea Wiarda
William Wieselquist

January 23, 2024

OAK RIDGE National Laboratory

ORNL IS MANAGED BY UT–BATTELLE, LLC, FOR THE U.S. DEPARTMENT OF ENERGY

ORNL/TM-2023/3201

Nuclear Energy and Fuel Cycles Division

PHOTONUCLEAR PHYSICS IN SCALE

Jesse Brown
Cihangir Celik
Thomas Evans
BK Jeon
Robert Lefebvre [2]
Jordan McDonnell
Katherine Royston
Dorothea Wiarda
William Wieselquist

Date Published: January 23, 2024

Prepared by
OAK RIDGE NATIONAL LABORATORY
Oak Ridge, TN 37831-6283
managed by
UT-Battelle, LLC
for the
US DEPARTMENT OF ENERGY
under contract DE-AC05-00OR22725

CONTENTS

LIST OF FIGURES . . . . . **iv**
LIST OF TABLES . . . . . **v**
ABBREVIATIONS . . . . . **vi**
ACKNOWLEDGEMENTS . . . . . **vii**
ABSTRACT **1**
1. Introduction **2**
2. Continuous-Energy Photonuclear Data **3**
3. Multigroup Photonuclear Data **6**
4. Enhanced Photon Physics **8**
    4.1 Atomic Relaxation Model 8
    4.2 Thick Target Bremsstrahlung Model 12
    4.3 Summary of Photon Data 27
5. Photon Transport with Photonuclear Reaction **31**
6. Isotope-wise Verification **33**
    6.1 Photon-induced problem 34
    6.2 Electron-induced problem 46
7. Conclusion **54**
8. Future Work **55**
References **55**
A. Walker Alias Sampling Method **A-1**
B. Numerical Integration Schemes **B-1**
    B.1 Cubic Spline Integration B-2
    B.2 Trapezoid Integration on Log-Log Scale B-2

LIST OF FIGURES

Figure 1. Atomic relaxation processes. . . . 9
Figure 2. Atomic relaxation probabilities for vacancies in the K-shell. . . . 9
Figure 3. Energies and probability radiative transition matrices for emission greater than 10 keV for $S_i = K, L1, L2, L3$ in (a–d). Shell indices for S_j are listed in Table 5. . . . 10
Figure 4. Energies and probability non-radiative transition matrices for emission greater than 10 keV for $S_i = K, L1, L2, L3$ in (a–d). . . . 11
Figure 5. Walker's alias sampling table for $Z = 82$ in (a) with the photon emission energies for each index listed in (b). . . . 12
Figure 6. Binding energy of subshells for $Z = 1$–98. . . . 13
Figure 7. Photoelectric cross sections for iron. . . . 14
Figure 8. Photoelectric subshell interaction CDF for tungsten. . . . 15
Figure 9. Compton scattering. . . . 15
Figure 10. Pair production. . . . 16
Figure 11. Pair production DCS for iron; (a) calculated and (b) sampled. . . . 19
Figure 12. Pair production PDF for μ. . . . 19
Figure 13. Scaled bremsstrahlung DCS for (a) Al and (b) Pb. . . . 21
Figure 14. Mass stopping powers from ESTAR for (a) Al and (b) Pb. . . . 22
Figure 15. Integrated mass stopping powers for Al, Pb, and SS304 steel. . . . 25
Figure 16. $P(T, E)$ matrix for steel. . . . 27
Figure 17. Bremsstrahlung yields for steel for 5 values for E_c. . . . 28
Figure 18. The bremsstrahlung (a) PDF and (b) CDF for steel. . . . 28
Figure 19. Comparison of sampled bremsstrahlung yields in steel for 6 different incident electron energies (T) compared to the analytic PDF. . . . 29

Figure 20. Relative error of photonuclear production with 15 MeV incident photon sources. . . . 36
Figure 21. Relative error of photonuclear production with 20 MeV incident photon sources. . . . 37
Figure 22. Relative error of photonuclear production with 30 MeV incident photon sources. . . . 38
Figure 23. Relative error of photonuclear production with 40 MeV incident photon sources. . . . 39
Figure 24. RMSRE of photon flux distribution with 20 MeV incident photon sources. . . . 41
Figure 25. RMSRE of neutron flux distribution with 20 MeV incident photon sources. . . . 42
Figure 26. RMSRE of photon flux distribution with 40 MeV incident photon sources. . . . 43
Figure 27. RMSRE of neutron flux distribution with 40 MeV incident photon sources. . . . 44
Figure 28. Relative error of multigroup photon flux distribution with 20 MeV incident photon sources for ^{235}U. . . . 45
Figure 29. RMSRE of photon flux distribution with 20 MeV incident photon sources (simplified photon physics in MCNP. . . . 45
Figure 30. Relative error of photonuclear production with 20 MeV incident electron sources. . . . 48
Figure 31. Relative error of photonuclear production with 40 MeV incident electron sources. . . . 49
Figure 32. RMSRE of photon flux distribution with 20 MeV incident electron sources. . . . 50
Figure 33. RMSRE of neutron flux distribution with 20 MeV incident electron sources. . . . 51
Figure 34. RMSRE of photon flux distribution with 40 MeV incident electron sources. . . . 52
Figure 35. RMSRE of neutron flux distribution with 40 MeV incident electron sources. . . . 53

Figure 36. Construction of Walker alias sampling table. . . . A-2
Figure 37. Sampling the unit square with a single random variate. . . . A-3

LIST OF TABLES

Table 2. Table of Energy Limits in ENDF/B-VII.1 Evaluations. 5

Table 3. The neutron boundary energies for the SCALE photonuclear multigroup library, with 31 neutron groups and 23 photon groups. 6

Table 4. The photon boundary energies for the SCALE photonuclear multigroup library, with 31 neutron groups and 23 photon groups. 7

Table 5. Index of electron shells for relaxation data. 10

Table 6. Data Sources Used for the SCALE Photon Enhanced Physics 29

Table 7. Processed Photon Data in `bremdata.h5` in the SCALE Data Distribution 30

Table 8. List of Isotopes in the ENDF/B-VII.1 SCALE Photonuclear Library 33

Table 9. Remarks on Isotopes with Differences in MCNP 34

ABBREVIATIONS

CDF	cumulative distribution function
CE	continuous-energy
DCS	differential cross section
ENDF	Evaluated Nuclear Data File
HEU	highly enriched uranium
LBE	lead–bismuth eutectic
LEU	low-enriched uranium
MC	Monte Carlo
MG	multigroup
NNSA	National Nuclear Security Administration
ORNL	Oak Ridge National Laboratory
PDF	probability distribution function
RMSRE	root mean squared relative error
TTB	thick-target bremsstrahlung

ACKNOWLEDGMENTS

Support for this research was provided by the US Department of Energy's (DOE's) National Nuclear Security Administration (NNSA), Office of Material Management and Minimization, Molybdenum-99 Program and by the Exascale Computing Project (17-SC-20-SC), a collaborative effort of the US DOE Office of Science and NNSA. Review and feedback by Noel B. Nelson and R. Blake Wilkerson are greatly appreciated.

ABSTRACT

Radiation shielding modeling involves a wide range of applications, such as power reactors, critical experiments, portable sources, linear accelerators, and fusion systems. Particle energy ranges vary from thermal energies to fast energy spectra. MAVRIC, as the radiation shielding sequence of the SCALE code system [1] developed and maintained by Oak Ridge National Laboratory, is capable of modeling both neutron and photon interactions in matter and is widely used by the US Nuclear Regulatory Commission, Department of Energy, the National Nuclear Security Administration, and radiation shielding practitioners all around the world. Although most applications don't involve highly energetic photons that can cause photonuclear reactions and create coupled chains of high energy, ionized electrons and bremsstrahlung radiation within a material medium, when present, these reactions can have a significant impact upon the downstream particle fluxes from incident photons above 20 MeV. For example, linear accelerators used for medical isotope production are examples of applications in which high-energetic photons are generated and used for driving or controlling other components of a complex facility. Radiation shielding analyses of such a facility would require accounting for any and all significant sources of radiation. Unfortunately, MAVRIC included no data and methods to model either photonuclear reactions or the bremsstrahlung photons until this work, which enabled accounting for both. Photonuclear reaction cross sections were imported from the Evaluated Nuclear Data File libraries, and corresponding methods were implemented in the SCALE code system; see Section 2 for how the nuclear data are imported and used. Bremsstrahlung photons were modeled by assuming thick-target approximation whereby all generated electrons and positrons due to photon interactions are assumed to be absorbed within the same material in which they were born, yielding a quick particle transport simulation method by using fast lookup tables for generating subsequent gammas; see Section 4 for details. A suite of verification models was used to test implemented methods and associated data. Tests yielded satisfactory results for the new features. Enhancements will be released as part of the next major SCALE release (v7.0), which is anticipated to be deployed in 2025, with beta releases available in the interim.

1. INTRODUCTION

Molybdenum-99 is crucial in medical diagnostics and serves as a key radioisotope used in more than 40,000 US medical procedures daily. Its decay product, ^{99m}Tc, aids in detecting heart disease and cancer, as well as in examining organs. Historically, the United States sourced most ^{99}Mo from abroad, with some produced using highly enriched uranium (HEU). HEU is a proliferation-sensitive material, and the prevention of its diversion or theft is a major concern due to its potential use as a component in nuclear weapons. To address this concern, the National Nuclear Security Administration (NNSA) established the ^{99}Mo program in 2012. The focus of the ^{99}Mo program is to provide support to facilities engaged in ^{99}Mo production, not only to aid them in the transition away from HEU-based process but also to establish domestic sources for ^{99}Mo. The ^{99}Mo program also pursues various ^{99}Mo production technologies with industry collaboration. Collaborators in the ^{99}Mo program incorporate electron linear accelerators to the ^{99}Mo production that are capable of inducing photonuclear reactions and low-enriched uranium (LEU) fission. Oak Ridge National Laboratory (ORNL) is offering research and development support, aiding in the design and licensing of technology [2]. To accurately predict the produced ^{99}Mo amount, the development of photonuclear production and electron transport capabilities to supplement the neutron and photon transport capabilities is essential. In this work, photonuclear production simulation capability within the SCALE/MAVRIC sequence was developed in response to the need for robust tools that estimate the ^{99}Mo production rates to support the objectives set by the NNSA, collaborators, and ORNL.

In the process of integrating photonuclear reactions into the SCALE transport sequences, new photonuclear libraries and enabling photonuclear physics in the photon transport simulation were required. Thus, the AMPX code was modified to work with the Evaluated Nuclear Data File (ENDF)/B-VII.1 photonuclear sublibrary. Subsequently, SCALE's radiation shielding module, MAVRIC, was enhanced to handle photonuclear reactions in its simulations, thanks to the introduction of a new photonuclear continuous-energy (CE) library. Early testing stages uncovered challenges with high-energy photons (> 20 MeV) in the photon simulation. High-energy photons triggered the generation of secondary electrons. These secondary electrons then led to further photon production by bremsstrahlung, creating an electron/photo cascade that posed computational challenges because SCALE lacked the capability for electron transport, which is essential eventually for accurately simulating these photon-induced electron interactions. To address this deficiency, the development of the thick-target bremsstrahlung (TTB) model and testing were undertaken. This model provides a reliable approximation of high-energy photon interactions, secondary electron generation, and the resulting photon production. To ensure the robustness and reliability of these enhancements, isotopic-wise verification was performed. These tests used incident photon/electron sources to evaluate the accuracy of data for each isotope. Given that high-energy photon interactions produce secondary electrons, the verification procedure was extended, and the TTB model was employed to clarify its accuracy in depicting electron-caused photon creation. Section 2 details the procedure and updates to generate new photonuclear CE library. Section 3 demonstrates enhancements carried out on the MAVRIC module and the TTB model employed. Section 4 presents various verification and validation results utilizing the developed photonuclear capabilities. Lastly, Section 5 summarizes the conclusions.

2. CONTINUOUS-ENERGY PHOTONUCLEAR DATA

The nuclear data processing code AMPX [3] is used to prepare nuclear data from the ENDF library for use in the SCALE code system. To incorporate photonuclear reactions in the SCALE transport sequences, the AMPX code needed several updates to process the ENDF/B-VII.1 photonuclear sublibrary [4]. The ENDF-formatted data files in the photonuclear sublibrary follow the same conventions as those of the neutron-induced reaction sublibrary. Reactions described within the files have corresponding reaction identification (MT) numbers. For example, MT=18 identifies neutron-induced fission in the neutron sublibrary, and it also identifies photofission in the photonuclear sublibrary. The photonuclear sublibrary ENDF files describe the one-dimensional cross sections as a function of incident photon energy in File 3 (MF=3) for each reaction present on the file. The AMPX module `polident` extracts that information and was able to store it in AMPX's own format without any updates. The kinematic data (two-dimensional data) can be stored in Files 4, 5, and 6, just as for the neutron sublibrary. As of SCALE 6.3.0, AMPX had the capability to process kinematic data for the following:

- Incident neutron, emitted neutron(s)
- Incident neutron, emitted photon(s)
- Incident photon, emitted photon(s) – photoatomic reactions only.

Several updates made to the AMPX sequences in this work enable the processing of kinematic data for the following:

- Incident photon, emitted neutron(s)
- Incident photon, emitted photon(s) – photonuclear reactions as well.

AMPX's `y12` sequence reads the kinematic data from the ENDF File 4, 5, or 6, and stores the results in AMPX's internal format. Before including the photonuclear reactions, the identity of the incident particle could be unambiguously deduced from the reaction identification. With the inclusion of photonuclear reactions, in which an incident neutron and incident photon reaction can have the same MT, the identity of the incident particle is now stored in the kinematic format during the `y12` sequence. The kinematic data in the ENDF photonuclear sublibrary include information about the identity and quantity of the particle emitted in a reaction. To include this information in AMPX's format, both $\gamma \rightarrow n$ and $\gamma \rightarrow \gamma$ categories of kinematic data are stored as yield data objects that store the multiplicity, angular distributions, and emitted particle energy distributions in the laboratory frame. To prepare for Monte Carlo sampling during CE transport, an additional summation reaction identifier is introduced to the photonuclear sublibrary files. As MT=1 represents the total cross section for neutron reactions, for SCALE CE photonuclear sublibrary files, an MT=1 is introduced to represent the total photon cross section, as the sum of photoatomic and photonuclear reaction cross sections. The newly introduced AMPX sequence `ce_simonize` writes the HDF5-based SCALE CE library that includes both the photonuclear sublibrary and external links to the original SCALE CE neutron and photoatomic library. The choice of externally linking the neutron and photoatomic library allows a user to load a single CE library file while preventing the duplication of data. The AMPX workflow that produces a SCALE CE library is as follows:

1. For each nuclide in the ENDF/B-VII.1 photonuclear sublibrary:
   (a) Read and store one-dimensional cross section data (`polident`)
   (b) Read and store two-dimensional kinematic data (`y12`)

(c) Compute probability distributions (`jamaican`)

(d) Produce a combined nuclide data file (`platinum`)

2. Combine all photonuclear nuclide files into a single HDF5 library file (`ce_ajax`)
3. Invoke `ce_simonize` to
   - Form the photonuclear MT=1 to represent the total photon cross section
   - Form the external links from the photonuclear library file to the original neutron and photoatomic library file

The result is a SCALE CE library that includes photonuclear data, ce_v7.1_photo, which can be specified as a SCALE cross section library in radiation shielding analysis inputs.

The AMPX sequences were updated for the Kalbach–Mann treatment of photons. According to the ENDF-6 manual [5], a photon evaluation file that specifies kinematic data in the Kalbach–Mann format must have its slope adjusted by

$$a_\gamma(E_\gamma, E_{b,cm}) = a_n(E_\gamma, E_{b,cm}) \sqrt{\frac{E_\gamma}{2m_n}} \min\left(4, \max\left(1, \frac{9.3}{\sqrt{E_{b,cm}}}\right)\right) \tag{1}$$

where a_n is the slope as computed for neutrons, E_γ is the incident photon energy, $E_{b,cm}$ is the energy of the emitted particle in the center-of-momentum reference frame, and m_n is the mass of the neutron, with E_γ, $E_{b,cm}$, and m_n in units of MeV. The double differential distribution must then be computed according to

$$f(\mu_{b,cm}, E_\gamma, E_{b,cm}) = \frac{f_0}{2}\left[(1-r) + r\frac{a}{\sinh a} e^{a\mu_{b,cm}}\right], \tag{2}$$

which differs from the expression for neutrons. In Eq. 2, $\mu_{b,cm}$ is the cosine of the scattering angle in the center-of-momentum reference frame, f_0 is the total emission probability, and r is the pre-compound fraction. Both f_0 and r are provided in the ENDF evaluation file for each incident and exit energy.

Another significant update was made to the two-body discrete reaction physics, which affected the MT=50 reaction channel in particular. For an incident neutron, MT=50 is not allowed in the ENDF format, and MT=2 is used instead for neutron elastic scattering. For an incident photon, the MT=50 reaction describes an exit channel in which the target is left in its ground state and a single neutron is emitted. Nevertheless, the probability of scattering into a given angle is conveyed in the ENDF evaluated data file in File 6, leaving the exit energy of the emitted neutron to be deduced by kinematics relationships. Previously, the kinematics relationships in AMPX assumed incident and emitted particles with the mass of a neutron. These kinematic relationships were updated to account for the incident photon being massless.

Some of the nuclide evaluations in the ENDF/B-VII.1 photonuclear sublibrary include cross sections and kinematics data for incident photon energies up to 150 MeV. Many evaluations, however, include data only up to 20 or 30 MeV. The list of the energy limits for each nuclide is shown in Table 2. To allow simulations to estimate photoneutron production for incident photon energies above this limit when needed, AMPX was updated to extrapolate the cross section and kinematic data. For this work, the last cross section and kinematic data are assumed to hold constant above the nuclide's existing data limit. Based on the cross-code comparison discussed below, this assumption seems to be consistent with the implementation in MCNP.

Before describing the cross-code comparison between the SCALE and MCNP implementations of photonuclear physics, it is necessary to identify differences in the nuclear data used by the two codes. Both codes begin with evaluated nuclear data from the ENDF/B-VII.1 photonuclear sublibrary.

Table 2. Table of Energy Limits in ENDF/B-VII.1 Evaluations. The upper energy limit (in MeV) is listed for each nuclide in the ENDF/B-VII.1 photonuclear sublibrary. The remaining nuclides in the library have upper energy limits of greater than 110 MeV.

Nuclide	ENDF Upper Energy (MeV)
Am-241	20
Np-237	20
Pu-238	20
Pu-239	20
Pu-240	20
Pu-241	20
Th-232	20
U-233	20
U-234	20
U-235	20
U-236	20
U-238	20
Be-9	30
H-2	30
V-51	30
W-180	30
W-182	30
W-183	30
W-186	30

SCALE uses nuclear data processed by AMPX into its CE data format; MCNP uses nuclear data processed by NJOY into the ACE ("A Compact ENDF") format.

One significant difference between the resulting SCALE photonuclear CE data library and the MCNP ACE library is the handling of fission neutrons in ^{241}Am. The ACE processed library neglects the photofission neutron distribution data for ^{241}Am [6]. Therefore, MCNP computations would include no neutron yield from fission events in ^{241}Am. The AMPX sequences, however, do obtain the photoneutron distribution data for ^{241}Am and store them in the SCALE CE data library. In turn, SCALE computations successfully produce a neutron yield from ^{241}Am photofission.

3. MULTIGROUP PHOTONUCLEAR DATA

In addition to modifying AMPX to process photonuclear data in the SCALE CE data format, we also performed the necessary updates to add photonuclear data to the multigroup (MG) data format.

The production of photons from neutrons was already included in the library format, in the form of transfer arrays that represent incident neutrons of a given energy group producing outgoing photons of the appropriate photon energy group. This work introduced additional transfer arrays that describe incident photons producing outgoing neutrons as a complementary capability. We also implemented the capability to include the ($\gamma \rightarrow n$) transfer into the total scattering matrix in the SCALE XSProc module.

In view of the objective to use the variance reduction capabilities of Denovo coupled with MAVRIC-Shift, we produced a coarse multigroup library based on the ENDF/B-VII.1 library. We started from the group boundaries of the SCALE 6.3.1 28 neutron + 19 photon groups library. Because several photonuclear evaluations extend to higher incident photon energies, we extended the group boundaries to 200 MeV for both incident neutrons and photons.

We chose 31 groups for neutrons and 23 groups for photons. When calculating the group coefficients for photons, we integrated with a weighting function of the $1/E$ form factor. This contrasts with the usual processing of SCALE multigroup libraries, in which the weighting function is a $1/E$ form factor cut off (set to zero) above 20 MeV. Using the $1/E$ form factor without a cut off enables the extension of the group boundaries to 200 MeV.

Group	Energy (eV)	Group	Energy (eV)
1	2.0000E+08	17	1.0677E+01
2	1.0000E+08	18	5.0000E+00
3	5.0000E+07	19	3.0590E+00
4	2.0000E+07	20	1.8554E+00
5	6.3763E+06	21	1.3000E+00
6	3.0119E+06	22	1.1253E+00
7	1.8268E+06	23	1.0000E+00
8	1.4227E+06	24	8.0000E-01
9	9.0718E+05	25	4.1399E-01
10	4.0762E+05	26	3.2500E-01
11	1.1109E+05	27	2.2500E-01
12	1.5034E+04	28	1.0000E-01
13	3.0354E+03	29	5.0000E-02
14	5.8295E+02	30	3.0000E-02
15	1.0130E+02	31	1.0000E-02
16	2.9023E+01		1.0000E-05

Table 3. The neutron boundary energies for the SCALE photonuclear multigroup library, with 31 neutron groups and 23 photon groups.

Group	Energy (eV)	Group	Energy (eV)
1	2.0000E+08	13	2.0000E+06
2	1.0000E+08	14	1.6600E+06
3	5.0000E+07	15	1.3300E+06
4	3.0000E+07	16	1.0000E+06
5	1.5000E+07	17	8.0000E+05
6	1.0000E+07	18	6.0000E+05
7	8.0000E+06	19	4.0000E+05
8	6.5000E+06	20	3.0000E+05
9	5.0000E+06	21	2.0000E+05
10	4.0000E+06	22	1.0000E+05
11	3.0000E+06	23	5.0000E+04
12	2.5000E+06		1.0000E+04

Table 4. The photon boundary energies for the SCALE photonuclear multigroup library, with 31 neutron groups and 23 photon groups.

4. ENHANCED PHOTON PHYSICS

The photon physics in the MAVRIC sequences in SCALE that use Monaco or Shift as the Monte Carlo (MC) solvers had several deficiencies related to secondary photon production from atomic relaxation and bremsstrahlung. In this work, models for both atomic relaxation and bremsstrahlung were added to the CE physics treatments in SCALE for use in both Shift and Monaco. The models and data for these processes were derived largely from Salvat [7] and Salvat and Fernández-Varea [8]. The TTB model is additionally based on the work of Kaltiaisenaho [9].

Sections 4.1 and 4.2 provide overviews of the physical processes and models adopted in the SCALE MC CE physics for atomic relaxation and TTB, respectively. A summary of the photon data added to SCALE data in this work is given in Section 4.3.

4.1 ATOMIC RELAXATION MODEL

Atomic relaxation occurs after the ejection of a bound electron by photoelectric absorption. There are two mechanisms by which energy is released in atomic relaxation, radiative and non-radiative, as illustrated in Figure 1. Radiative emission occurs when a vacancy in shell i is filled with an electron from a higher (less energetic) shell j, $S_j \rightarrow S_i$. The energy is carried away by an isotropically emitted photon with energy

$$E_{ij} = U_i - U_j \,, \tag{3}$$

where U_i is the binding energy of shell S_i. The resulting transition leaves a new vacancy in S_j.

Non-radiative emission occurs when a vacancy in shell i is filled with an electron in shell j and the resulting energy is carried away by an electron in shell k, $S_j \rightarrow S_i \Rightarrow S_k$. The energy carried away by the electron is

$$T_{ijk} = U_i - U_j - U_k \,. \tag{4}$$

The resulting transition leaves two vacancies in (S_j, S_k).

Data for atomic relaxation data are given in Deslattes *et al.* [10] and Perkins *et al.* [11]. We note here that the observed values of E and T differ slightly from the predicted formulas in Eqs. (3) and (4) due to binding effects and other material-dependent phenomenon. The probabilities of radiative and non-radiative atomic relaxation transitions for K-shell electrons are illustrated in Fig. 2. The data show that non-radiative events represent an increasingly small percentage of transitions above $Z \sim 40$. Furthermore, $L2$ and $L3$ transitions account for the bulk of the radiative event relaxation photons.

In SCALE MC applications, we are generally interested only in photon transport that is greater than 10 keV. We can write the radiative and non-radiative energy and probability matrices as $\mathbf{E}_p(S_i)$ and $\mathbf{P}_p(S_i)$ with $p = \mathrm{r}, \mathrm{nr}$, respectively. The elements of the matrices are defined as follows:

$$\begin{aligned}
[\mathbf{E}_\mathrm{r}(S_i)]_{nj} &= E_{ij} \in Z_n \,, \\
[\mathbf{E}_\mathrm{nr}(S_i)]_{nj} &= \max_k T_{ijk} \in Z_n \,, \\
[\mathbf{P}_\mathrm{r}(S_i)]_{nj} &= p(S_j \rightarrow S_i) \in Z_n \,, \\
[\mathbf{P}_\mathrm{nr}(S_i)]_{nj} &= \sum_k p(S_j \rightarrow S_i \Rightarrow S_k) \in Z_n \,.
\end{aligned}$$

These matrices are plotted in Figs. 3 and 4. For radiative emission, only $S_i = K$ results in both significant photon emission greater than 10 keV and probabilities greater than 10 %. For non-radiative probabilities, the

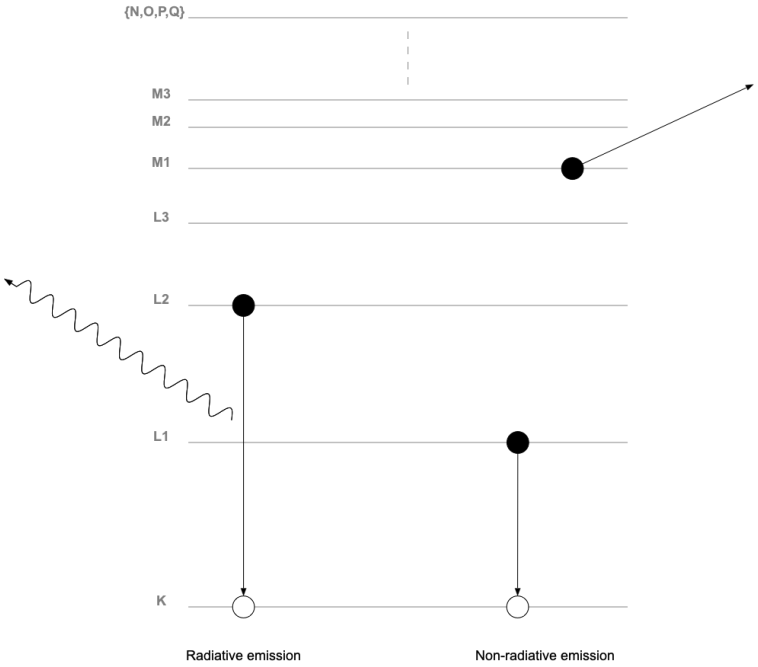

Figure 1. Atomic relaxation processes.

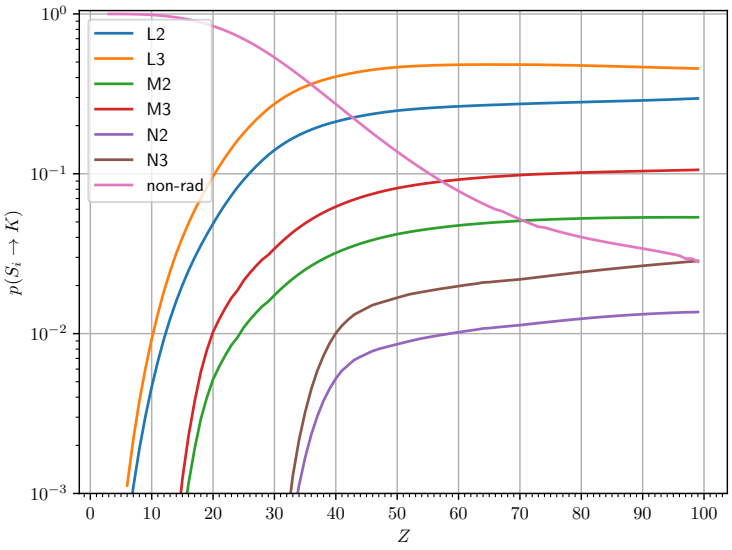

Figure 2. Atomic relaxation probabilities for vacancies in the *K*-shell. All non-radiative relaxation is summed across all shells.

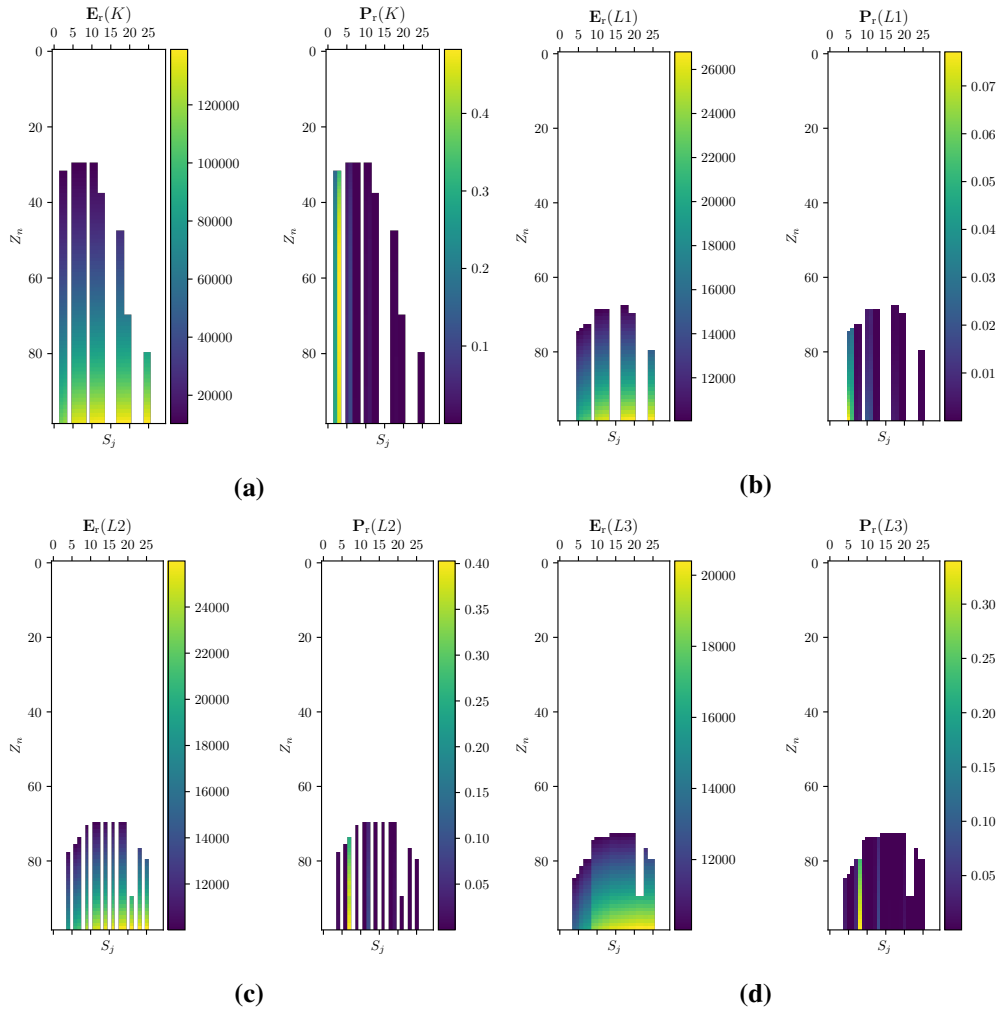

Figure 3. Energies and probability radiative transition matrices for emission greater than 10 keV for $S_i = K, L1, L2, L3$ in (a–d). Shell indices for S_j are listed in Table 5.

Table 5. Index of electron shells for relaxation data.

shell	index	shell	index	shell	index
K	0	N2	10	O5	20
L1	1	N3	11	O6	21
L2	2	N4	12	O7	22
L3	3	N5	13	P1	23
M1	4	N6	14	P2	24
M2	5	N7	15	P3	25
M3	6	O1	16	P4	26
M4	7	O2	17	P5	27
M5	8	O3	18	Q1	28
N1	9	O4	19	outer	29

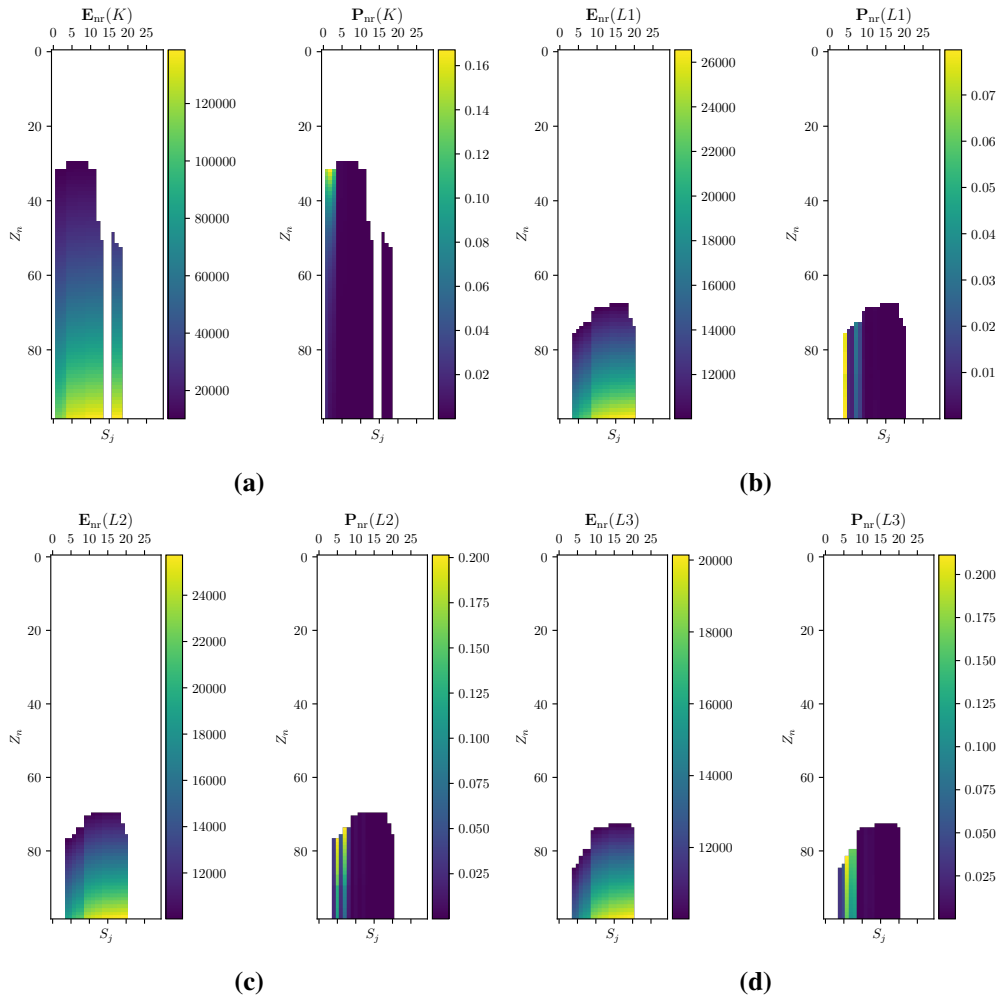

Figure 4. Energies and probability non-radiative transition matrices for emission greater than 10 keV for $S_i = K, L1, L2, L3$ in (a–d). Shell indices for S_j are listed in Table 5.

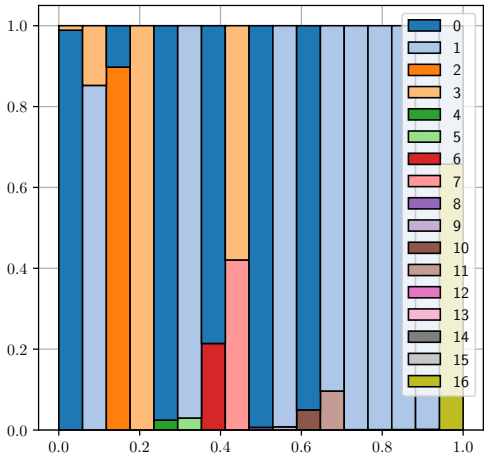

(a)

Bin index/Emission energy (eV)			
0	94 650.8	8	115 332.0
1	98 431.6	9	115 375.0
2	110 416.0	10	115 851.0
3	111 295.0	11	115 907.0
4	112 009.0	12	115 998.0
5	112 009.0	13	116 006.0
6	114 846.0	14	116 076.0
7	115 080.0	15	116 085.0
8	115 332.0	16	0

(b)

Figure 5. Walker's alias sampling table for $Z = 82$ in (a) with the photon emission energies for each index listed in (b). All radiative and non-radiative events are samples in $n = 16$ that yields a photon with energy 0 keV.

electron emission for all shells never exceeds 12 % probability, and those that do (K-shell) result in electrons with energies less than 20 keV. Thus, our implementation of atomic relaxation in SCALE considers only K-shell radiative emission.

Atomic relaxation for K-shell vacancies are sampled using pre-computed tables and Walker's alias [7] sampling method; see Appendix A for details of the methodology. Transition data for $Z = 1$–98 are compiled and Walker alias sampling tables are constructed giving the emission probabilities and energies. All non-radiative and radiative transitions yielding emissions lower than 10 keV are lumped into a single probability that yields an emission energy of 0 eV since we are ignoring these events. This provides a fair game when sampling relaxation from vacancies in the K-shell. An example of the Walker sampling table for $Z = 82$ is illustrated in Fig. 5.

4.2 THICK TARGET BREMSSTRAHLUNG MODEL

Bremsstrahlung radiation results when energetic free electrons are deflected in the electric field of an atomic nucleus. The resulting photons can have a significant impact on the overall photon flux in neutron/photon transport problems. However, because simulating full electron transport is orders of magnitude more computationally expensive than neutron and photon MC transport, we use an approximate model, known as the thick-target bremsstrahlung (TTB) approximation, to incorporate photons without performing full electron transport. The TTB model incorporated into SCALE CE MC physics is based heavily on the work of Kaltiaisenaho [9] and uses data and physics models described in Salvat [7], Salvat and Fernández-Varea [8], and Seltzer and Berger [12]. A summary of all the TTB data is given in Section 4.3.

The TTB model requires two enhancements to the photon CE MC physics in SCALE:

- The calculation of secondary electron energies from photoelectric, Compton (incoherent) scattering, and pair production events.
- Sampling bremsstrahlung photons from the resulting energetic electrons.

These are covered in Sections 4.2.1 and 4.2.2, respectively.

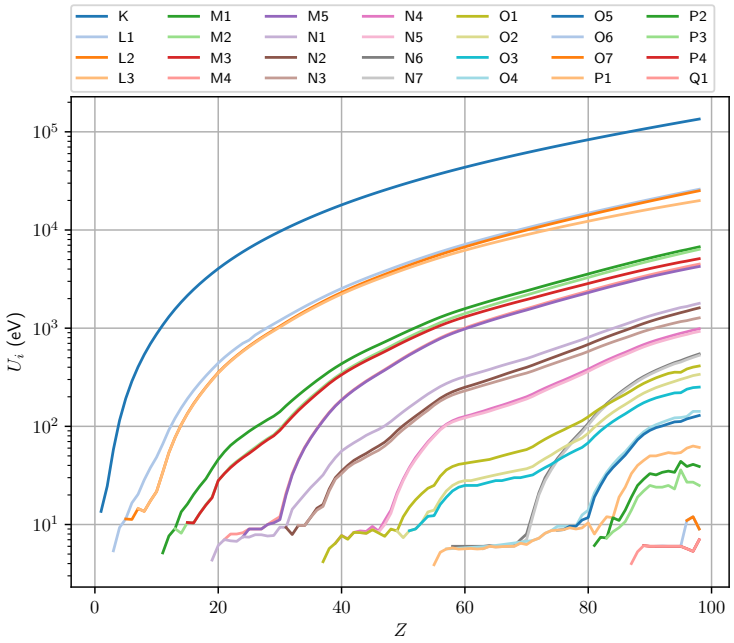

Figure 6. Binding energy of subshells for $Z = 1$–98.

4.2.1 CALCULATION OF SECONDARY ELECTRONS

4.2.1.1 Photoelectric Interactions

The energy of the secondary electron from a photoelectric interaction with subshell S_i is given by

$$T = E - U_i \,, \tag{5}$$

where T is the electron energy, E is the incident photon energy, and U_i is the binding energy of S_i. Binding energies for $Z = 1$–98 are shown in Fig. 6 [13]. The direction of the electron is approximated by the direction of the incoming photon.

To determine the subshell for a given photoelectric event, the cross sections must be sampled. This can add an unacceptable level of computational cost because the cross sections for each subshell must be calculated, which can be as high as 39 cross section lookups. However, an approximation can be employed by analyzing the photoelectric cross sections. For example, Fig. 7 shows the photoelectric cross sections for each subshell in iron. We see that the variation of the electron cross sections above the K-shell binding energy (7117 eV) is roughly constant. Thus, we can build pre-computed sampling tables over bins specified by the binding energy of each subshell.

To begin, an initial energy grid is calculated:

$$\{U_{\min}, U_n, U_{n-1}, \ldots, U_0, U_{\max}\} \,,$$

where n is the index of the highest shell for the element with $U_n > U_{\min}$, and U_0 is the K-shell binding energy. Here, we set $U_{\min} = 1$ keV and $U_{\max} = 1$ GeV. The algorithm then proceeds in two parts. First, the average subshell cumulative distribution functions (CDFs) are calculated in the range above U_0 as follows:

1. Starting at U_0, calculate the CDF from the photoelectric cross sections on uniformly spaced logarithmic points over the range $[U_0, U_{\max}]$;

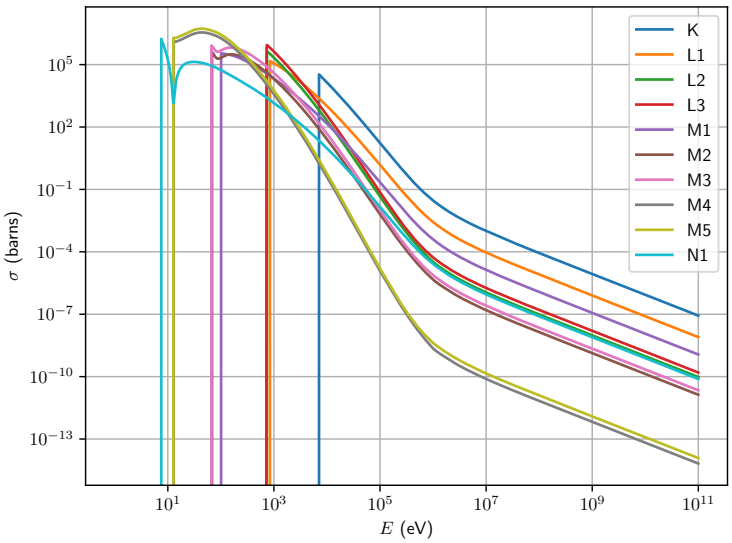

Figure 7. Photoelectric cross sections for iron.

2. calculate the linear least squares solution overall CDFs that has slope m_i for shell i;
3. if $\max_{0<i<n} |m_i| > 10^{-4}$, then advance the grid to the next energy point (U_*) and return to 2;
4. set the CDF for each subshell i to $m_i \log U_* + b_i$;
5. insert U_* into the energy grid.

The resulting grid now is defined as follows:

$$\{U_n, U_{n-1}, \ldots, U_0, U_*, U_{\max}\} .$$

To determine the average CDF in each bin, randomly sample each photoelectric subshell reaction in each bin in the grid from U_n to U_*. This yields a set of discrete CDFs for each element over all photoelectric subshell reactions that can be quickly sampled without requiring any additional cross section lookups during transport. An example of the resulting grid for tungsten is shown in Fig. 8.

4.2.1.2 Compton Scattering

Compton (i.e., incoherent) scattering is shown Fig. 9. The energy of the emitted electron, assuming that the target is at rest, is given by [14]

$$T = E - E' . \tag{6}$$

The angle of the secondary electron is given by

$$\cot\varphi = \left(1 + \frac{E}{m_e c^2}\right) \tan\frac{\theta}{2} , \tag{7}$$

where $m_e c^2$ is the electron rest mass energy.

4.2.1.3 Pair Production

The pair production interaction is shown in Fig. 10. The total energy balance for pair production is

$$E = T^+ + T^- + 2m_e c^2 . \tag{8}$$

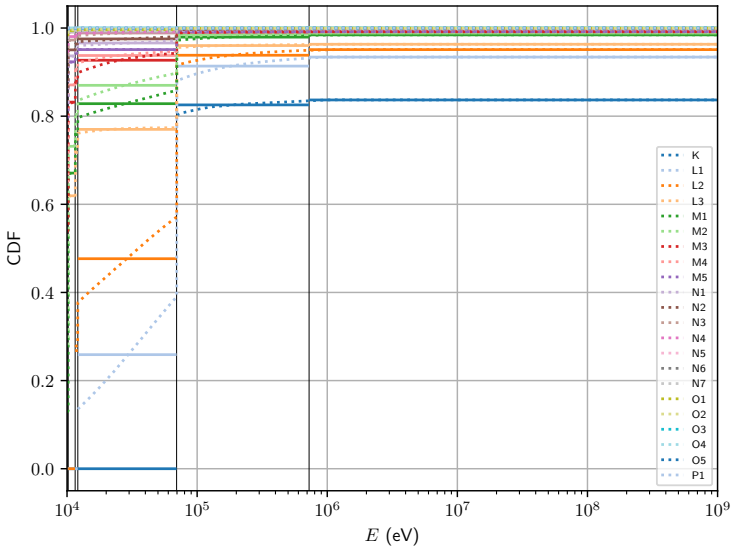

Grid point	Energy (eV)	Subshell
U_{min}	1.0000×10^4	
U_3	1.0209×10^4	$L3$
U_2	1.1546×10^4	$L2$
U_1	1.2103×10^4	$L1$
U_0	6.9529×10^4	K
U_*	7.2512×10^5	
U_{max}	1.0000×10^9	

Figure 8. Photoelectric subshell interaction CDF for tungsten. The grid boundaries are shown by black vertical lines. In each bin the averaged subshell CDF is shown by solid lines, and the true CDF across the bin is given by dotted lines.

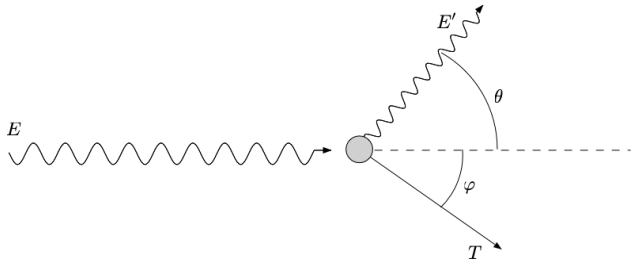

Figure 9. Compton scattering.

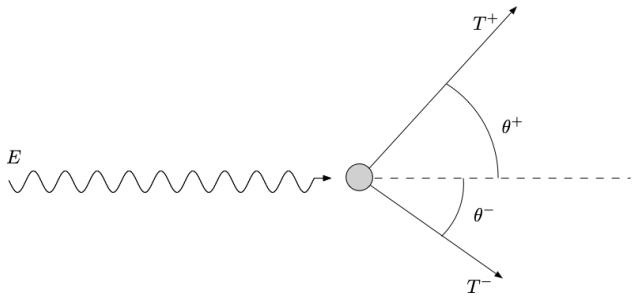

Figure 10. Pair production.

Defining the reduced electron energy as

$$\epsilon = \frac{T^- + m_e c^2}{E} , \tag{9}$$

the electron/positron energies are

$$T^- = \epsilon E - m_e c^2 , \tag{10}$$

$$T^+ = (1-\epsilon)E - m_e c^2 . \tag{11}$$

This yields two limits corresponding to $T^\pm = 0$, giving a reduced energy range of $[\epsilon_{\min}, \epsilon_{\max}]$,

$$\epsilon_{\min} = \frac{m_e c^2}{E} = \frac{1}{k} , \tag{12}$$

$$\epsilon_{\max} = \frac{E - m_e c^2}{E} = 1 - \frac{1}{k} = 1 - \epsilon_{\min} . \tag{13}$$

Following the methodology of Salvat [7] the Bethe–Heitler differential cross section (DCS) neglecting triplet production and including an empirical low-energy correction term to ensure positivity (F_0) and a high-energy radiative correction is

$$\frac{d\sigma_{\rm pp}}{d\epsilon} = r_e^2 \alpha Z^2 C_r \frac{2}{3}\left[2\left(\frac{1}{2} - \epsilon\right)^2 \phi_1(\epsilon) + \phi_2(\epsilon)\right] . \tag{14}$$

Here, Z is atomic number, r_e is the classical electron radius,

$$r_e = \frac{e^2}{m_e c^2} = 2.817\,940\,326\,7 \times 10^{-15}\ \text{m} , \tag{15}$$

and α is the fine-structure constant,

$$\alpha = \frac{e^2}{\hbar c} = \frac{1}{137.035\,999\,074} . \tag{16}$$

The constant $C_r = 1.0093$ is the high-energy radiative correction limit, and

$$\phi_1(k,\epsilon) = \frac{1}{2}(3\Phi_1(k,\epsilon) - \Phi_2(k,\epsilon)) - 4f_C(Z) + F_0(k,Z) , \tag{17}$$

$$\phi_2(k,\epsilon) = \frac{1}{4}(3\Phi_1(k,\epsilon) + \Phi_2(k,\epsilon)) - 4f_C(Z) + F_0(k,Z) . \tag{18}$$

The high-energy Coulomb correction, f_C, is given by

$$\begin{aligned} f_C(Z) = a^2[&(1+a^2)^{-1} + 0.202\,059 - 0.036\,93a^2 + 0.008\,35a^4 \\ &- 0.002\,01a^6 + 0.000\,49a^8 - 0.000\,12a^{10} + 0.000\,03a^{12}] , \end{aligned} \tag{19}$$

where $a = \alpha Z$. The empirical low-energy correction is

$$F_0(k,Z) = (-1.744 - 12.10a + 11.18a^2)(2/k)^{1/2} + (8.523 + 73.26a - 44.41a^2)(2/k) \\ - (13.52 + 121.1a - 96.41a^2)(2/k)^{3/2} + (8.946 + 62.05a - 63.41a^2)(2/k)^2 \,. \tag{20}$$

And (Φ_1, Φ_2) are given by

$$\Phi_1(k,\epsilon) = 2 - 2\ln(1+b^2) - 4b\arctan(b^{-1}) + 4\ln\Big(\frac{Rm_ec}{\hbar}\Big)\,, \tag{21}$$

$$\Phi_2(k,\epsilon) = \frac{4}{3} - 2\ln(1+b^2) + 2b^2[4 - 4b\arctan(b^{-1}) - 3\ln(1+b^{-2})] + 4\ln\Big(\frac{Rm_ec}{\hbar}\Big)\,, \tag{22}$$

where $Rm_ec/\hbar$ is the reduced screening radius, and

$$b = \frac{Rm_ec}{\hbar}\frac{1}{2k}\frac{1}{\epsilon(1-\epsilon)}\,. \tag{23}$$

As stated above, the reduced energy is distributed between

$$\epsilon \in [\epsilon_{\rm min}, \epsilon_{\rm max}]\,, \tag{24}$$

and we drop the dependence of ϕ_i on k, $\phi_i(\epsilon) \equiv \phi_i(k,\epsilon)$. Equation (14) is equivalent to the probability distribution function (PDF) and can be written (neglecting normalization) in the form

$$\frac{d\sigma_{\rm pp}}{d\epsilon} \equiv p_{\rm pp}(\epsilon) = 2\Big(\frac{1}{2} - \epsilon\Big)^2\phi_1(\epsilon) + \phi_2(\epsilon)\,. \tag{25}$$

Here, we note that $(\phi_1, \phi_2) \geq 0$ and

$$\max\phi_i(\epsilon) = \phi_i(1/2)\,, \quad i = 1,2\,. \tag{26}$$

The PDF, $p_{\rm pp}$, can be expressed in the following form for sampling via the composition and rejection methods (see Section 1.2 in [7]),

$$p_{\rm pp}(\epsilon) = u_1U_1(\epsilon)\pi_1(\epsilon) + u_2U_2(\epsilon)\pi_2(\epsilon)\,, \tag{27}$$

with

$$u_1 = \frac{2}{3}\Big(\frac{1}{2} - \frac{1}{k}\Big)^2\phi_1(1/2)\,, \tag{28}$$

$$\pi_1(\epsilon) = \frac{3}{2}\Big(\frac{1}{2} - \frac{1}{k}\Big)^{-3}\Big(\frac{1}{2} - \epsilon\Big)^2\,, \tag{29}$$

$$U_1(\epsilon) = \frac{\phi_1(\epsilon)}{\phi_1(1/2)}\,. \tag{30}$$

Moreover,

$$u_2 = \phi_2(1/2)\,, \tag{31}$$

$$\pi_2(\epsilon) = \frac{1}{2}\Big(\frac{1}{2} - \frac{1}{k}\Big)^{-1}\,, \tag{32}$$

$$U_2(\epsilon) = \frac{\phi_2(\epsilon)}{\phi_2(1/2)}\,. \tag{33}$$

The sampling procedure for ϵ is as follows:

1. Sample $i = (1, 2)$ according to probabilities (ξ_1)

$$p(1) = \frac{u_1}{u_1 + u_2} \,, \tag{34}$$

$$p(2) = \frac{u_2}{u_1 + u_2} \,. \tag{35}$$

2. Sample ϵ from π_i using the inverse transform method:

$$\xi = \int_{\epsilon_{\min}}^{\epsilon} \pi_i \, d\epsilon' \,, \tag{36}$$

which yields,

$$\epsilon = \begin{cases} \frac{1}{2} + (\frac{1}{2} - \frac{1}{k})(2\xi_2 - 1)^{1/3} \,, & i = 1 \,, \\ \frac{1}{k} + (\frac{1}{2} - \frac{1}{k}) 2\xi_2 \,, & i = 2 \,. \end{cases} \tag{37}$$

3. If $\xi_3 > U_i(\epsilon)$, then go to 1, else accept ϵ.

When $i = 1$, the term $(2\xi_2 - 1)$ can be less than zero, which presents no problems mathematically since $\forall \mathcal{R}$, $\sqrt[3]{-x} = -y$; however, the standard C++ function `std::pow(-x, 1/3)` will yield `-nan`. Therefore, it is necessary to use `std::cbrt` in SCALE, which will give the correct behavior. Once ϵ is known, then the energies of the (e^-, e^+) pair can be calculated using Eqs. (10) and (11).

To sample the polar angle of the (e^-, e^+) pair, we use the following PDF:

$$p(\mu^\pm) = a(1 - \beta^\pm \mu^\pm)^{-2} \,, \tag{38}$$

where $\mu^\pm = \cos\theta^\pm$, and $\beta^\pm$ is the ratio of the electron/positron velocity to the speed of light,

$$\beta^\pm = \frac{\sqrt{T^\pm (T^\pm + 2m_0c^2)}}{T^\pm + m_0c^2} \,. \tag{39}$$

Normalizing the PDF (through change of variables $u = 1 - \beta\mu$),

$$1 = \int_{-1}^{1} a(1 - \beta\mu)^{-2} \, d\mu = -\frac{a}{\beta} \int_{1+\beta}^{1-\beta} u^{-2} \, du \,, \tag{40}$$

gives

$$\frac{\beta}{a} = \frac{1}{1-\beta} - \frac{1}{1+\beta} \,. \tag{41}$$

Inverting to solve for ξ yields

$$\xi = -\frac{a}{\beta} \int_{1+\beta}^{1-\beta\mu} u^{-2} \, du = \frac{a}{\beta} u^{-1} \Big|_{1+\beta}^{1-\beta\mu} \,. \tag{42}$$

Solving for μ gives

$$\mu^\pm = \frac{(2\xi - 1) + \beta^\pm}{(2\xi - 1)\beta^\pm + 1} \,. \tag{43}$$

The pair production DCS given by Eq. (14) is shown for iron in Fig. 11a. Sampled results produced using the method described above are shown in Fig. 11b. The sampling scheme correctly reproduces the PDF for the reduced electron energy. The PDF for μ given in Eq. (38) is shown in Fig. 12.

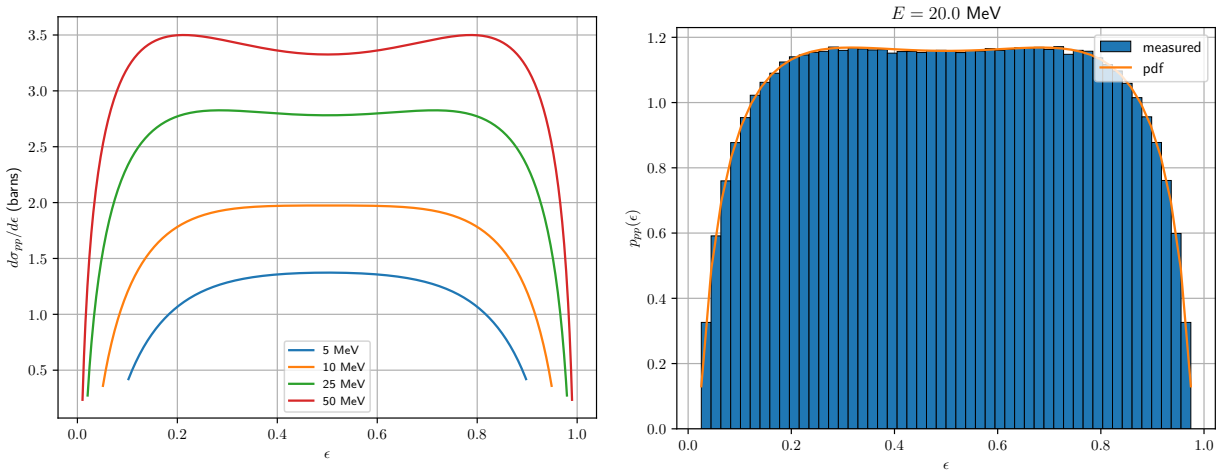

(a) **(b)**

Figure 11. Pair production DCS for iron; (a) calculated and (b) sampled.

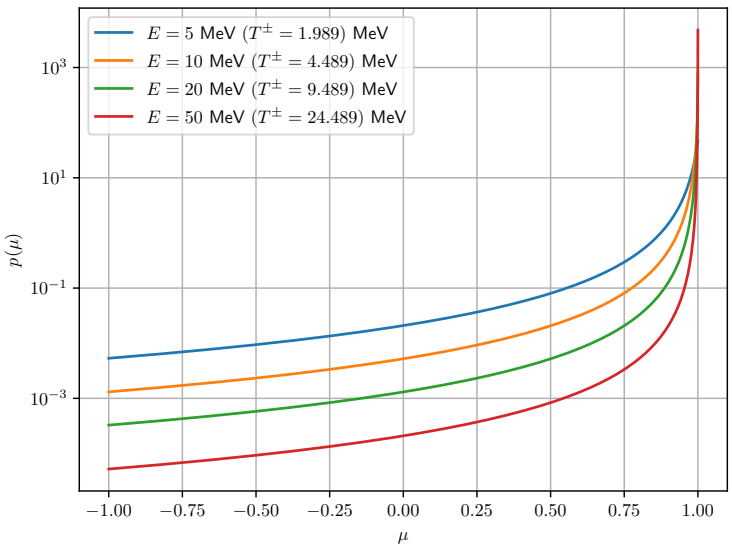

Figure 12. Pair production PDF for μ.

4.2.2 TTB PHOTON SAMPLING

Having defined methods for calculating the secondary electron and positron energies and angles in Section 4.2.1, the techniques for estimating the bremsstrahlung emission from those charged particles are outlined here. The TTB approximation that we adapted for use in SCALE follows the methodology developed by Kaltiaisenaho [9]. In summary, we sample the number of bremsstrahlung photons emitted from an energetic (e^-, e^+) using a continuous slowing down approximation. The TTB approximation *assumes* that the charged particle will come to rest in the medium where it is created; thus, it will be accurate only in regions where the particle range is less than the thickness of the material medium in which it is created. In thin shells, a significant amount of energy can escape the medium, and in this case the TTB will overestimate the bremsstrahlung photon production.

4.2.2.1 Bremsstrahlung Cross Section and Stopping Power

The DCS for bremsstrahlung is [15]

$$\frac{d\sigma_{\text{br}}}{dE} = \frac{Z^2}{\beta^2}\frac{1}{E}\chi(Z,T,\kappa)\,, \tag{44}$$

where

$$\begin{aligned} E &= \text{photon energy}\,,\\ T &= \text{electron energy}\,,\\ Z &= \text{atomic number}\,,\\ \chi &= \text{scaled bremsstrahlung cross section (barn)}\,, \end{aligned} \tag{45}$$

and

$$\kappa = \frac{E}{T}\,. \tag{46}$$

β is the ratio of the electron velocity to the speed of light given in Eq. (39). The scaled bremsstrahlung cross section is

$$\chi(Z,T,\kappa) = \frac{\beta^2}{Z^2}E\frac{d\sigma_{\text{br}}}{dE}\,. \tag{47}$$

The scaled DCS for Z = 1–99 was compiled in Seltzer and Berger [16] using a κ grid of 32 points. Figure 13 shows the scaled bremsstrahlung DCS for aluminum and lead. These data are available in digital form through the Penelope code distribution [7].

Stopping power is defined

$$S(T) \triangleq -\frac{dT}{ds} = N\int W\frac{d\sigma}{dW}\,dW\,, \tag{48}$$

where N is the number density in atoms barn^{-1} cm^{-1} and W is the particle energy. Stopping power has both radiative (bremsstrahlung) and collisional (ionization/excitation) components; the total is defined as follows:

$$S_{\text{tot}}(T) = S_{\text{col}}(T) + S_{\text{rad}}(T)\,. \tag{49}$$

Using Eq. (48), the radiative stopping power due to bremsstrahlung is thus

$$S_{\text{rad}}(T) = N\frac{Z^2}{\beta^2}\int_0^T \chi(Z,T,\kappa)\,dE\,. \tag{50}$$

Because $\kappa = E/T$, we have $dE = Td\kappa$, and

$$S_{\text{rad}}(T) = N\frac{Z^2}{\beta^2}T\int_0^1 \chi(Z,T,\kappa)\,d\kappa\,. \tag{51}$$

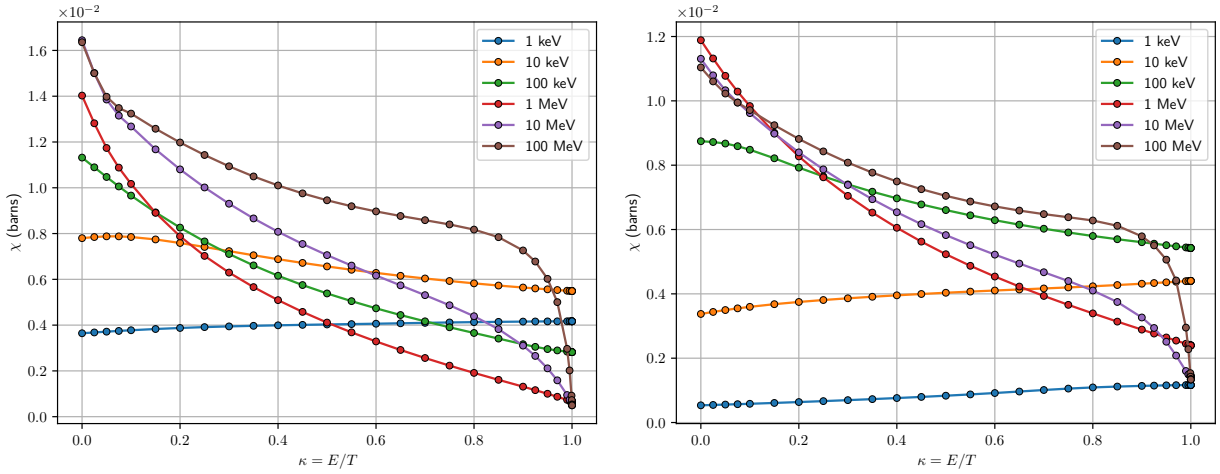

Figure 13. Scaled bremsstrahlung DCS for (a) Al and (b) Pb.

Naturally,

$$N = \frac{N_A \rho}{M} \,, \tag{52}$$

where N_A is Avogadro's number in units of atoms barn^{-1} cm^{-1}, M is the mass in g mol^{-1}, and ρ is the density in g cm^{-3}. The mass stopping power is defined as follows:

$$\text{mass stopping power} \triangleq \frac{1}{\rho} S(T) \,. \tag{53}$$

Then

$$\frac{1}{\rho} S_{\text{rad}}(T) = \frac{N_A}{M} \frac{Z^2}{\beta^2} T \int_0^1 \chi(Z, T, \kappa)\, d\kappa \,. \tag{54}$$

Mass stopping powers are available for Z = 1–99 through the ESTAR database [17]. Figure 14 shows tabulated stopping powers for aluminum and lead. The stopping powers are tabulated on a 97-point energy grid.

4.2.2.2 Continuous Slowing Down Approximation

The range of a particle as it slows down from $T \to 0$ is

$$R(T) = \int_0^T \left(\frac{dT'}{ds} \right)^{-1} dT' = \int_0^T \frac{1}{S_{\text{tot}}(T')}\, dT' \,. \tag{55}$$

Similarly, the radiation energy emitted as bremsstrahlung during the path is

$$E_{\text{br}}(T) = \int_0^{R(T)} \left(\frac{dT'}{ds} \right)_{\text{rad}} ds \,. \tag{56}$$

Because $ds = (dT'/ds)^{-1}\, dT'$, we have

$$E_{\text{br}}(T) = \int_0^T \left(\frac{dT'}{ds} \right)_{\text{rad}} \left(\frac{dT'}{ds} \right)^{-1} dT' = \int_0^T \frac{S_{\text{rad}}(T')}{S_{\text{tot}}(T')}\, dT' \,. \tag{57}$$

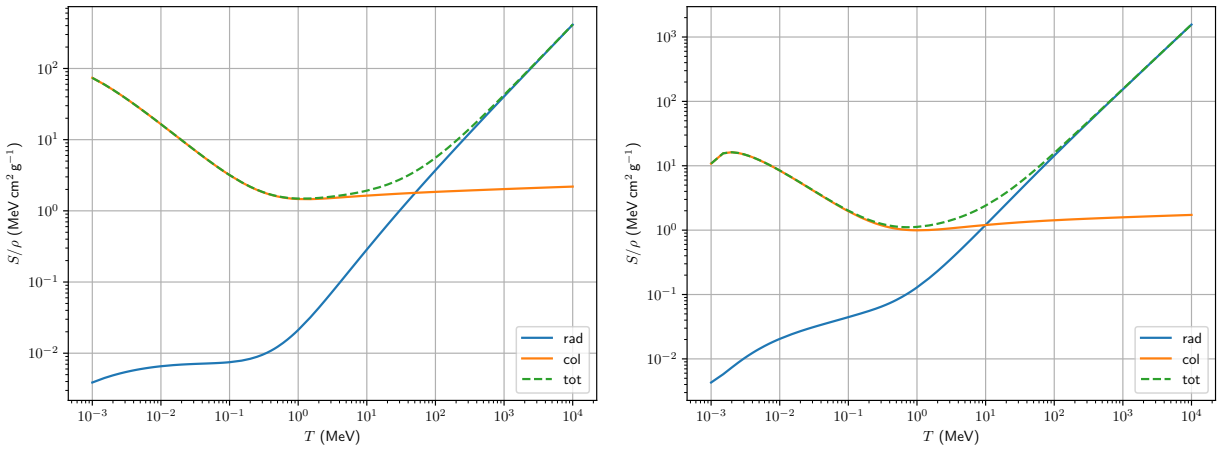

Figure 14. Mass stopping powers from ESTAR for (a) Al and (b) Pb.

The fraction of total energy emitted as bremsstrahlung, the radiative yield, is

$$Y_{\rm rad}(T) = \frac{E_{\rm br}}{T} = \frac{1}{T}\int_0^T \frac{S_{\rm rad}(T')}{S_{\rm tot}(T')}\,dT' \,. \tag{58}$$

The mean free path is defined as follows:

$$\lambda = \frac{1}{N\sigma}\,, \tag{59}$$

which has units of cm per collision. The average number of bremsstrahlung photons emitted per unit path length is thus given by $\lambda_{\rm br}^{-1}$, the inverse bremsstrahlung mean free path,

$$\lambda_{\rm br}^{-1}(T) = N\sigma_{\rm br}(T)\,, \tag{60}$$

and

$$\sigma_{\rm br}(T) = \int_0^T \frac{d\sigma_{\rm br}}{dE}\,dE \,. \tag{61}$$

Recall from Eq. (44) that $d\sigma_{\rm br}/dE \propto E^{-1}$; thus, we must adjust the lower limit of integration to a cutoff value, $E_{\rm c}$,

$$\sigma_{\rm br}(T) \equiv \sigma_{\rm br}(T, E_{\rm c}) = \int_{E_{\rm c}}^T \frac{d\sigma_{\rm br}}{dE}\,dE = \frac{Z^2}{\beta^2}\int_{E_{\rm c}}^T \frac{1}{E}\chi(Z,T,\kappa)\,dE \tag{62}$$

Transforming to $d\kappa$ as in Eq. (51),

$$\sigma_{\rm br}(T, E_{\rm c}) = \frac{Z^2}{\beta^2}\int_{\kappa_{\rm c}}^1 \frac{1}{\kappa}\chi(Z,T,\kappa)\,d\kappa\,, \tag{63}$$

and $\kappa_{\rm c} = E_{\rm c}/T$. Thus, we have for $\lambda_{\rm br}^{-1}$,

$$\lambda_{\rm br}^{-1}(T, E_{\rm c}) = N\frac{Z^2}{\beta^2}\int_{\kappa_{\rm c}}^1 \frac{1}{\kappa}\chi(Z,T,\kappa)\,d\kappa \,. \tag{64}$$

The number of photons with energy, $E > E_{\rm c}$, is given by integrating over the inverse mean free path,

$$Y_{\rm n}(T, E_{\rm c}) = \int_{R(E_{\rm c})}^{R(T)} \lambda_{\rm br}^{-1}(T', E_{\rm c})\,ds \,. \tag{65}$$

Transforming this equation using $ds = S_{\text{tot}}(T')^{-1}dT'$ as in Eq. (57) gives

$$Y_{\text{n}}(T, E_{\text{c}}) = \int_{E_{\text{c}}}^{T} \frac{\lambda_{\text{br}}^{-1}(T', E_{\text{c}})}{S_{\text{tot}}(T')}\, dT' \,. \tag{66}$$

4.2.2.3 Monte Carlo Implementation

After defining the fundamental physical equations for bremsstrahlung processes in Sections 4.2.2.1 and 4.2.2.2, they must be formulated into a TTB model that can be used within CE MC transport codes. The following steps are required:

1. Generate stopping powers for material compounds.
2. Generate bremsstrahlung sampling tables for each material.
3. Define a sampling algorithm for bremsstrahlung emission.

The first step is to calculate stopping powers for material compounds. We can use the Bragg's additivity rule [9] to obtain the bremsstrahlung DCS for a compound using Eq. (44) as follows:

$$\frac{d\sigma_{\text{br}}}{dE} = \frac{1}{\beta^2 E} \sum_j \gamma_j Z_j^2 \chi(Z_j, T, \kappa) \,. \tag{67}$$

The atom number density for *nuclide* j in atoms $\text{barn}^{-1}\,\text{cm}^{-1}$ is

$$N_j = \gamma_j N = w_j \frac{\rho N_{\text{A}}}{M_j} \,, \tag{68}$$

where γ_j is the atom fraction and w_j is the weight fraction of consituent j. Additionally, $N = \sum_j N_j$, so

$$\frac{1}{M} = \sum_j \frac{w_j}{M_j} \,. \tag{69}$$

Using the definition of the stopping power Eq. (48) and inserting Eq. (67) gives

$$\begin{aligned} S_{\text{rad}}(T) &= N \int_0^T \frac{1}{\beta^2} \sum_j \gamma_j Z_j^2 \chi(Z_j, T, \kappa)\, dE \\ &= \sum_j N \gamma_j \frac{Z_j^2}{\beta^2} T \int_0^1 \chi(Z_j, T, \kappa)\, d\kappa \,. \end{aligned} \tag{70}$$

Substituting the number density of nuclide j gives

$$\frac{1}{\rho} S_{\text{rad}}(T) = \sum_j \frac{w_j}{M_j} \frac{N_{\text{A}} Z_j^2}{\beta^2} T \int_0^1 \chi(Z_j, T, \kappa)\, d\kappa \,. \tag{71}$$

The radiative mass stopping power for each nuclide j in units of $\text{eV}\,\text{cm}^2\,\text{mol}^{-1}$ is

$$\left(\frac{1}{\rho} S_{\text{rad}}\right)_j = \frac{N_{\text{A}} Z_j^2}{\beta^2} T \int_0^1 \chi(Z_j, T, \kappa)\, d\kappa \,. \tag{72}$$

Furthermore, the material radiative mass stopping power is

$$\frac{1}{\rho}S_{\text{rad}}(T) = \sum_j \frac{w_j}{M_j}\left(\frac{1}{\rho}S_{\text{rad}}\right)_j . \tag{73}$$

For the collisional stopping power, we will make an approximation and use the Bragg's additivity rule there as well. This is not rigorously correct since we are neglecting density factor and electron excitation effects [12, 18]. Incorporating these effects and using the Bethe stopping power formula directly to calculate collisional stopping power for compounds will be part of future work.

The collisional stopping power tables from the ESTAR database [17] are per *element*, so we need to normalize by M_e:

$$\frac{1}{M_e} = \sum_{i=1}^{n_e} \frac{w_i}{M_i} , \tag{74}$$

where n_e is the number of constituent nuclides in element e. Thus,

$$\left(\frac{1}{\rho}S_{\text{col}}\right)_j \overset{j\in e}{=} M_e\left(\frac{1}{\rho}S_{\text{rad}}\right)_e . \tag{75}$$

Then, we calculate the composition's mass collisional stopping power as above:

$$\frac{1}{\rho}S_{\text{col}}(T) = \sum_j \frac{w_j}{M_j}\left(\frac{1}{\rho}S_{\text{col}}\right)_j . \tag{76}$$

Note here that if we have a composition consisting of a single element, we simply return the element's stopping power because all $j \in e$:

$$\frac{1}{\rho}S_{\text{col}}(T) = \sum_j \frac{w_j}{M_j}\left(\frac{1}{\rho}S_{\text{col}}\right)_j = \left(\sum_j \frac{w_j}{M_j}\right)M_e\left(\frac{1}{\rho}S_{\text{rad}}\right)_e = \left(\frac{1}{\rho}S_{\text{rad}}\right)_e . \tag{77}$$

The total stopping power is given in Eq. (49).

For all TTB data, we use a uniform logarithmic energy grid containing 200 points defined over the range 10^3–10^9 eV. The collisional stopping powers from the ESTAR database and the bremsstrahlung scaled DCS (Eq. (47)) from Seltzer and Berger [16] are interpolated onto this grid using cubic spline interpolation. Equation (72) is evaluated using the trapezoid numerical integration rule. Integrated stopping powers for aluminum, lead, and SS304 steel are shown in Fig. 15. The elemental values for aluminum and lead were compared to ESTAR data, and good agreement was shown—thereby confirming the accuracy of the cubic spine interpolation and trapezoid rule integration scheme.

To calculate bremsstrahlung photon yields, we need to integrate the inverse mean free path defined in Eq. (64). Using the Bragg additivity rule for the DCS from Eq. (67) and rearranging gives

$$\begin{aligned}
\lambda_{\text{br}}^{-1}(T, E_{\text{c}}) &= N\int_{E_{\text{c}}}^{T} \frac{1}{\beta^2 E}\sum_j \gamma_j Z_j^2 \chi(Z_j, T, \kappa)\, dE \\
&= \int_{E_{\text{c}}}^{T} \frac{1}{\beta^2 E}\sum_j N_j Z_j^2 \chi(Z_j, T, \kappa)\, dE \\
&= \int_{E_{\text{c}}}^{T} \frac{1}{\beta^2 E}\sum_j w_j \frac{\rho N_A}{M_j} Z_j^2 \chi(Z_j, T, \kappa)\, dE .
\end{aligned} \tag{78}$$

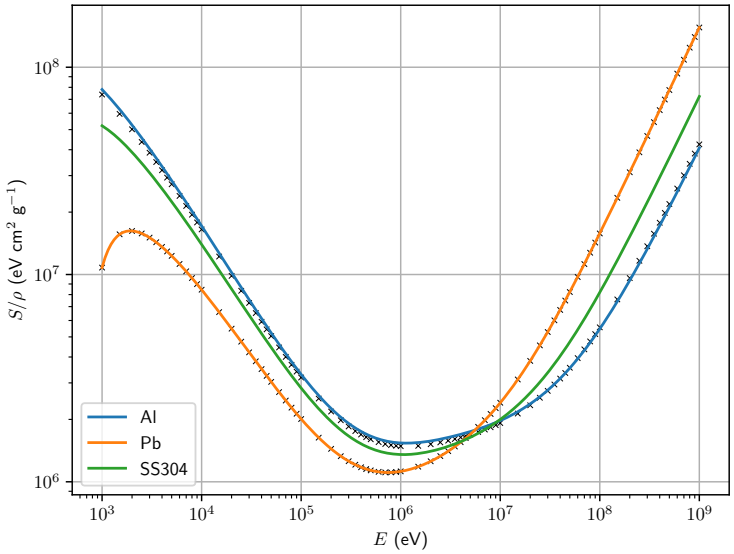

Figure 15. Integrated mass stopping powers for Al, Pb, and SS304 steel. The Al and Pb values are compared to the raw data from the ESTAR database.

The composition-scaled DCS is defined as follows:

$$\bar{\chi}(T,\kappa) = \sum_j \frac{w_j N_A Z_j^2}{M_j} \chi(Z_j, E, \kappa) \,. \tag{79}$$

This gives the following for the inverse mean free path

$$\frac{1}{\rho}\lambda_{\text{br}}^{-1}(T, E_c) = \frac{1}{\beta^2}\int_{E_c}^{T} \frac{1}{E}\bar{\chi}(T,\kappa)\, dE \,. \tag{80}$$

Returning to Eq. (66), these can be used to determine the number of bremsstrahlung photon emitted between E_1 and E_2:

$$n_p(T,E) = Y_n(T,E_1) - Y_n(T,E_2) \,, \quad E_1 > E > E_2 > E_c \,. \tag{81}$$

Written another way, we can define the PDF for sampling a photon with energy E' as

$$p(T,E)dE = Y_n(T,E+dE) - Y_n(T,E) = P\{E \le E' \le E + dE\} \,. \tag{82}$$

From the definition of the derivative,

$$\frac{dY_n}{dE} = \lim_{dE\to 0} \frac{Y_n(E+dE) - Y_n(E)}{dE} = p(T,E) \,. \tag{83}$$

Now, substituting Eq. (80) into Eq. (66),

$$Y_n(T,E) = \int_E^T dT' \int_E^T \frac{\frac{1}{\beta^2 E'}\bar{\chi}(T',\kappa')}{\frac{1}{\rho}S_{\text{tot}}(T')} dE' \,, \tag{84}$$

and changing the order of integration

$$Y_n(T,E) = \int_E^T dE' \int_E^T \frac{\frac{1}{\beta^2 E'}\bar{\chi}(T',\kappa')}{\frac{1}{\rho}S_{\text{tot}}(T')} dT' \,. \tag{85}$$

Using Eqs. (83) and (85), we apply the fundamental theorem of calculus to arrive at our final result for the PDF for the emission of photons with energy E by an electron with energy T,

$$p(T,E) = \frac{dY_{\rm n}}{dE} = \int_E^T \frac{\frac{1}{\beta^2 E}\bar{\chi}(T',\kappa)}{\frac{1}{\rho}S_{\rm tot}(T')}\,dT' \,. \tag{86}$$

The CDF is then given by Eq. (85):

$$P(T,E) = \int_E^T p(T,E)\,dE = Y_n(T,E) \,. \tag{87}$$

Having defined the number yield, PDF, and CDF, an algorithm for bremsstrahlung photon emission can be formulated. First, the yields (85), PDF (86), and CDF (87) are calculated using a 200-point logarithmic energy grid for both T and E. The steps for sampling the photons from bremsstrahlung are as follows.

1. Sample the number of photons:
$$n = \lfloor Y(T) + \xi \rfloor \,, \tag{88}$$
where $(Y(T) = Y_n(T, E = 1\,\text{keV})$ via Eq. (85) and $0 \le \xi \le 1$.

2. Because interpolating the PDF in T is expensive, sample to determine the bin, $T_i = \{T_k, T_{k+1}\}$. Using the composition method, the PDF is
$$p(T_i,E) = f_k p(T_k,E) + f_{k+1} p(T_{k+1},E) \,, \tag{89}$$
where the probabilities are defined in log ($\log \equiv \log_e$) space,
$$f_k = \frac{\log T_{k+1} - \log T}{\log T_{k+1} - \log T_k} \,, \tag{90}$$
$$f_{k+1} = \frac{\log T - \log T_k}{\log T_{k+1} - \log T_k} \,. \tag{91}$$

3. Because the PDF and CDF are unnormalized, find the maximum CDF, $P_{\rm max}$ defined below in Eq. (96), on the selected grid $i \in \{k, k+1\}$ such that
$$P_{\rm max} = \begin{cases} P(T_i,T_i) & i = k \\ P(T_i,T_{i-1}) < P_{\rm max} < P(T_i,T_i) & i = k+1 \end{cases} \,. \tag{92}$$

4. Sample the photon energy bin E_j according to
$$P(T_i,E_j) \le \xi P_{\rm max} \le P(T_i,E_{j+1}) \,. \tag{93}$$
Linear interpolation on a log-log scale is used to calculate E,
$$E = E_j\left((1+c_j)\frac{\xi P_{\rm max} - P(T_i,E_j)}{E_j p(T_i,E_j)} + 1\right)^{\frac{1}{1+c_j}} \,, \tag{94}$$
where
$$c_j = \frac{\log p(T_i,E_{j+1}) - \log p(T_i,E_j)}{\log E_{j+1} - \log E_j} \,. \tag{95}$$

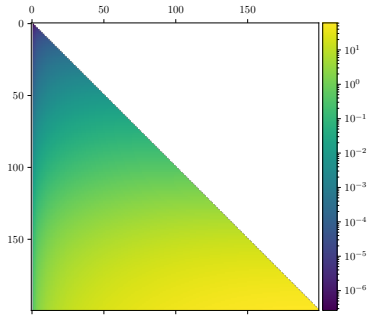

Figure 16. *P*(*T*, *E*) matrix for steel. The dimensions of the matrix correspond to the 200 point logarithmic energy grid.

In this case, $c_j \neq 1$, which indicates a PDF that went as E^{-1}. Additionally, the log-log interpolation can, through numerical roundoff, result in photon energies outside the bin—that is, $E > E_{j+1}$. This is handled in the code by setting

```
E = std::min(E, grid[j+1]);
```

The maximum CDF, $P_{\max}$, is required to prevent interpolation resulting in $E > T$ that can occur when $i = k + 1$ via Eq. (92). Written as a square matrix, $[\mathbf{P}]_{mn} = P(T_m, E_n)$, $\mathbf{P}$ is lower triangular, as shown in Fig. 16. Thus, the maximum CDF for T_i will be at $P(T_i, T_i)$, and when $i = k + 1$ the energy bin spans $[P(T_{k+1}, T_k), P(T_{k+1}, T_{k+1})]$. Equation (94) for this case is

$$T = T_k \left((1 + c_k) \frac{P_{\max} - P(T_{k+1}, T_k)}{T_k p(T_{k+1}, T_k)} + 1 \right)^{\frac{1}{1+c_k}} ,$$
$$c_k = \frac{\log p(T_{k+1}, T_{k+1}) - \log p(T_{k+1}, T_k)}{\log T_{k+1} - \log T_k} .$$

Solving for $P_{\max}$ gives

$$P_{\max} = P(T_{k+1}, T_k) + \frac{\exp((\log T - \log T_k)(1 + c_k)) - 1}{1 + c_k} T_k p(T_{k+1}, T_k) . \tag{96}$$

Equations (85) to (87) are all calculated using the same integration scheme. The integral over dT is performed using cubic spline integration, and the integral over dE is performed using trapezoidal integration on a log-log grid; see Appendix B for details. Figure 17 shows the yields for different values of E_c for steel. The PDF and CDF for steel are shown in Fig. 18. To show the correctness of the sampling scheme, we compare the measured bremsstrahlung yields for 6 incident electron energies versus the integrated PDFs in Fig. 19. Our bremsstrahlung implementation correctly preserves the theoretical PDFs defined by Eq. (86).

4.3 SUMMARY OF PHOTON DATA

Digital data for the enhanced photon physics are taken from two sources: the ESTAR database [17] and the Penelope code distribution [7]. The source data are summarized in Table 6. These data are pre-processed using the methodologies described in Sections 4.1 and 4.2 into a `bremdata.h5` file that is distributed with the SCALE data distribution. The processed data in `bremdata.h5` are summarized in Table 7.

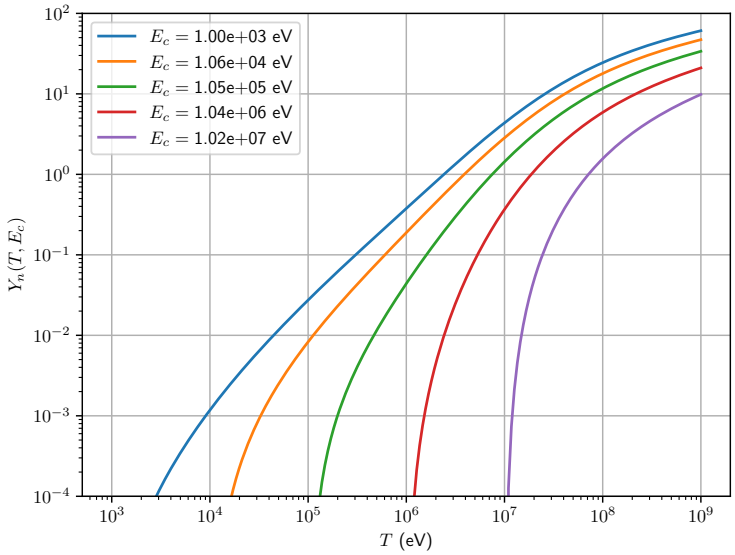

Figure 17. Bremsstrahlung yields for steel for 5 values for E_c.

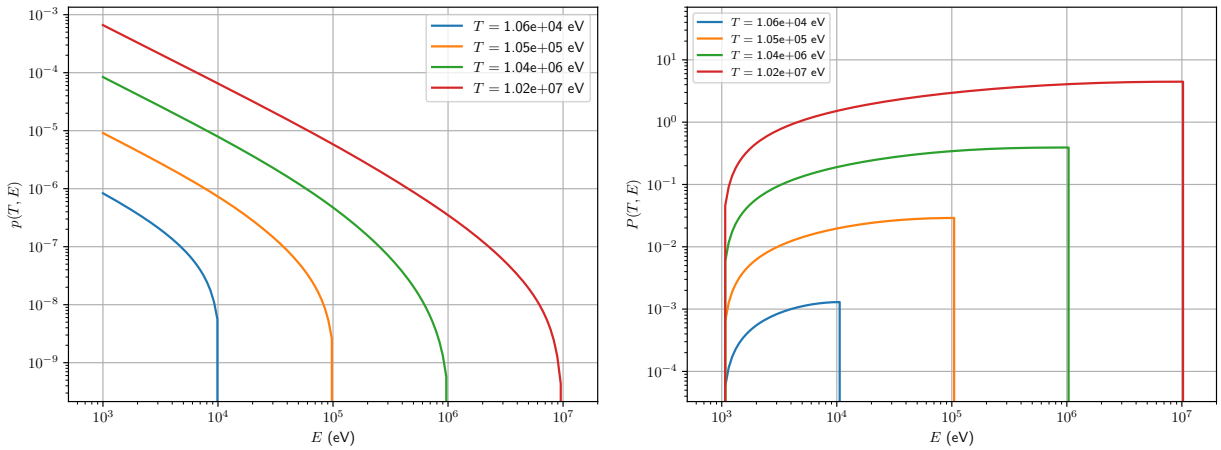

(a) **(b)**

Figure 18. The bremsstrahlung (a) PDF and (b) CDF for steel.

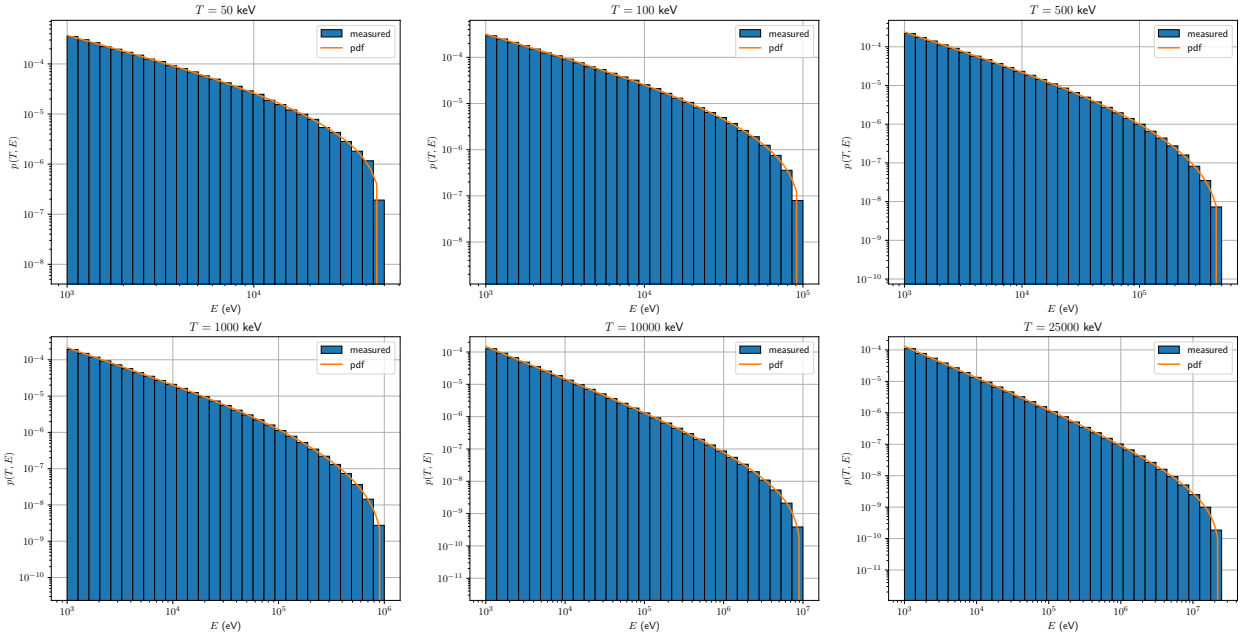

Figure 19. Comparison of sampled bremsstrahlung yields in steel for 6 different incident electron energies (T) compared to the analytic PDF.

Table 6. Data Sources Used for the SCALE Photon Enhanced Physics

Source	Description
ESTAR	Mass stopping powers, S_{col}, S_{rad}, and S_{tot}, in MeV cm^2 g^{-1} on a 97 point energy grid in MeV for Z = 1–98 [17].
Penelope	Binding energies in eV for Z = 1–98 for 39 subshells [13].
Penelope	Reduced screening radius ($Rm_{\text{e}}c/\hbar$) for Z = 1–98 [7].
Penelope	Atomic relaxation radiative transition energies and probabilities for $S_j \rightarrow K$ transitions in which the emission photon is greater than 10 keV. All non-radiative transitions and radiative transitions less than 10 keV are lumped into a probability that returns a 0 eV photon (since we are not transporting below this boundary in the code). [10, 11]
Penelope	Differential cross sections in barns on a 57-point incident electron energy grid in MeV and a reduced energy ($\kappa = T/E$) grid of 32 points [16].

Table 7. Processed Photon Data in `bremdata.h5` in the SCALE Data Distribution

HDF5 Group	Data	Dimensions	Description
/	energy_grid	[200]	200 point logarithmic spaced energy grid over range 10^3–10^9 eV.
/	kappa	[32]	32-point reduced energy grid $\kappa = T/E$.
/	Scol	[98, 200]	Mass collisional stopping power for Z = 1–98 on 200 point energy grid in eV cm^2 g^{-1}.
/	Srad	[98, 200]	Mass radiative stopping power for Z = 1–98 on 200 point energy grid in eV cm^2 mol^{-1}.
/	dcs	[98, 200, 32]	Scaled differential bremsstrahlung cross sections for Z = 1–98 on a 200 point incident electron energy grid for 32 reduced energy points in barns.
electron_shells	mt	[39]	MT reaction ENDF ids for electron subshell photoelectric reactions.
electron_shells	shell	[39]	Electron shell string descriptors for MT subshell reactions.
electron_shells	Eb	[98, 39]	Electron subshell binding energies for Z = 1–98 in eV.
pe_sampling_tables/z	grid	[n]	n-point energy grid for the photoelectric subshell CDF in eV for Z = 1–98.
pe_sampling_tables/z	mts	[m]	m subshell photoelectric reaction MTs for Z = 1–98.
pe_sampling_tables/z	cdf	[$n-1, m$]	subshell photoelectric CDF for $n-1$ energy bins and m subshell reactions for Z = 1–98.
pair_production	screening_radius	[98]	reduced screening radius ($Rm_e c/\hbar$) for Z = 1–98.
relaxation_data/z	E	[n]	radiative transition energies from shells $S_j \rightarrow K$ in eV.
relaxation_data/z	walker_bin	[n, 2]	Walker Alias sampling bins in range $[0, n)$ for each column, n of the unit-sampling square.
relaxation_data/z	walker_prob	[n]	Walker Alias sampling probabilities for each column, n, of the unit-sampling square.

5. PHOTON TRANSPORT WITH PHOTONUCLEAR REACTION

MAVRIC is the main radiation shielding analysis tool in SCALE and is used extensively for a wide range of applications and by a variety of practitioners. It is a 3D MC code capable of using both multigroup (MG) and CE nuclear data libraries. The MAVRIC code uses Monaco [19] as the MC engine, the *Robus* module to load data, and the *Physica* transport engine to perform particle interactions with materials for CE libraries. Both Robus and Physica reside in the *Exnihilo* suite and are also used by the *Shift* particle transport code. New source code implementations and updates have been performed to allow and control the loading of photonuclear reaction data and interpreting them during particle transport calculations. Although MAVRIC is the main product for radiation shielding analysis, *MAVRIC-Shift* has also been released with SCALE since v6.3.0 and supports parallel processing of shielding analysis with proven variance reduction methods of CADIS [20] and FW-CADIS [21]. MAVRIC and MAVRIC-Shift sequences are both enabled to support the photonuclear reactions with the TTB approximation since both use the same CE nuclear data loading and physics mechanisms. The MAVRIC-Shift sequence has also been updated to support angular distributions other than isotropic distribution by implementing user-defined histograms and discrete distributions in source definitions via funded activity for another project.

MAVRIC input parameters have been updated to accommodate photonuclear reactions and the TTB approximation. The SCALE code base has been updated to support photonuclear reactions when CE libraries are used, whereas support for MG libraries is currently not available. A new keyword named "*usePhotonuclear*" was added to the parameters block to enable the photonuclear reactions, which are disabled by default. Another keyword to toggle the TTB, named "*noTTB*," was also implemented to disable the TTB approximation, which is enabled by default. An example parameters block to enable photonuclear reaction is shown below in Listing 1. An update to fission particle generation was also performed to provide flexibility to control photon-induced fission events (photofissions). Neutrons born from fission events, both neutron- and photon-induced, are controlled via the "*fissionMult*" keyword which can have an integer value of 0 (no fission neutrons), 1 (generate fission neutrons only born from neutron-induced fission events), 2 (*default* behavior: generate both neutron- and photon-induced fission neutrons), or 3 (generate fission neutrons only born from photofissions). Photons from fission events are controlled via "*secondaryMult*" keyword, which can have an integer value of 0 (no secondary photons from any reaction), 1 (generate secondary photons from scattering and capture events and not from fission events), or 2 (*default* behavior: generate secondary photons from all reactions).

Listing 1 Example parameters blocks for enabling photonuclear reactions.

```
'  Photonuclear reactions and TTB are enabled
 read parameters
       perBatch=100000  batches=100
       ceLibrary="ce_v7.1_photo.h5"
       usePhotonuclear
 end parameters
```

```
'  Photonuclear reactions are enabled while TTB is disabled
read parameters
      perBatch=100000  batches=100
       ceLibrary="ce_v7.1_photo.h5"
      usePhotonuclear
      noTTB
end parameters
```

6. ISOTOPE-WISE VERIFICATION

As mentioned in the introduction, the goal of new photonuclear capability in SCALE/MAVRIC is to estimate ^{99}Mo amount yields in the light-water reactor UO_2 assemblies, leveraging electron linear accelerator technology. Because of the absence of electron transport simulation in SCALE, a hybrid methodology was adopted for the assessment, using both SCALE and the MCNP codes. This section details a systematic verification sequence for the combined MCNP/SCALE approach. A detailed verification of each isotope in the photonuclear library was carried out by comparing results from MCNP6.2 and SCALE/MAVRIC using homogeneous problems. The primary objective of this verification was to examine the SCALE photonuclear library and transport capability by comparing the total photonuclear production and multigroup photon and neutron flux of SCALE/MAVRIC with the one of MCNP 6.2. The ENDF/B VII.1 library includes 163 isotopes with photonuclear data. To examine the accuracy of the photonuclear library data at different energy ranges, the incident energy for the photon and electron source was adjusted between 15 to 40 MeV. It is important to note that SCALE/MAVRIC handles only photon/neutron transport calculations; thus, the photon/neutron flux distribution obtained from the MCNP6.2 electron transport simulation was fed into the SCALE/MAVRIC calculations. Photonuclear production was compared for 154 of the 163 isotopes. Nine isotopes were omitted from the comparison because they lacked either ENDF/B/VII.1 neutron or photonuclear library libraries in MCNP 6.2. The photonuclear sublibrary remained unchanged from ENDF/B-VII.0. Tables 8 and 9 show the isotopes available in the ENDF/B-VII.1 SCALE photonuclear library and those left out for isotope-wise verification, respectively. It is important to mention that during this test, probability tables to treat the resonance cross sections in the unresolved resonance energy range were not utilized for MCNP and MAVRIC simulations because some nuclides in the MCNP ENDF/B-VII.1 library lack these tables, whereas AMPX has them. Carbon (^{12}C, ^{13}C) was treated as elemental because both MCNP and SCALE provide elemental neutron cross sections. To avoid the supercritical fixed source problem with the fissile isotope, the neutron generation by fission was suppressed to isolate the photonuclear effect only.

Table 8. List of Isotopes in the ENDF/B-VII.1 SCALE Photonuclear Library

Isotope								
^{2}H	^{36}S	^{53}Cr	^{70}Ge	^{95}Mo	^{113}Cd	^{126}Te	^{181}Ta	^{240}Pu
^{9}Be	^{35}Cl	^{54}Cr	^{72}Ge	^{96}Mo	^{114}Cd	^{128}Te	^{180}W	^{241}Pu
^{12}C	^{37}Cl	^{55}Mn	^{73}Ge	^{97}Mo	^{116}Cd	^{130}Te	^{182}W	^{241}Am
^{13}C	^{36}Ar	^{54}Fe	^{74}Ge	^{98}Mo	^{112}Sn	^{127}I	^{183}W	
^{14}N	^{38}Ar	^{56}Fe	^{76}Ge	^{100}Mo	^{114}Sn	^{129}I	^{184}W	
^{15}N	^{40}Ar	^{57}Fe	^{84}Sr	^{102}Pd	^{115}Sn	^{133}Cs	^{186}W	
^{16}O	^{40}Ca	^{58}Fe	^{86}Sr	^{104}Pd	^{116}Sn	^{135}Cs	^{197}Au	
^{17}O	^{42}Ca	^{59}Co	^{87}Sr	^{105}Pd	^{117}Sn	^{137}Cs	^{206}Pb	
^{18}O	^{43}Ca	^{58}Ni	^{88}Sr	^{106}Pd	^{118}Sn	^{141}Pr	^{207}Pb	
^{23}Na	^{44}Ca	^{60}Ni	^{90}Sr	^{107}Pd	^{119}Sn	^{144}Sm	^{208}Pb	
^{24}Mg	^{46}Ca	^{61}Ni	^{90}Zr	^{108}Pd	^{120}Sn	^{147}Sm	^{209}Bi	
^{25}Mg	^{48}Ca	^{62}Ni	^{91}Zr	^{110}Pd	^{122}Sn	^{148}Sm	^{232}Th	
^{26}Mg	^{46}Ti	^{64}Ni	^{92}Zr	^{107}Ag	^{124}Sn	^{149}Sm	^{233}U	
^{27}Al	^{47}Ti	^{63}Cu	^{93}Zr	^{108}Ag	^{121}Sb	^{150}Sm	^{234}U	
^{28}Si	^{48}Ti	^{65}Cu	^{94}Zr	^{109}Ag	^{123}Sb	^{151}Sm	^{235}U	
^{29}Si	^{49}Ti	^{64}Zn	^{96}Zr	^{106}Cd	^{120}Te	^{152}Sm	^{236}U	
^{30}Si	^{50}Ti	^{66}Zn	^{93}Nb	^{108}Cd	^{122}Te	^{154}Sm	^{238}U	
^{32}S	^{51}V	^{67}Zn	^{94}Nb	^{110}Cd	^{123}Te	^{158}Tb	^{237}Np	
^{33}S	^{50}Cr	^{68}Zn	^{92}Mo	^{111}Cd	^{124}Te	^{159}Tb	^{238}Pu	
^{34}S	^{52}Cr	^{70}Zn	^{94}Mo	^{112}Cd	^{125}Te	^{165}Ho	^{239}Pu	

Table 9. Remarks on Isotopes with Differences in MCNP

Reason for Difference in MCNP ENDF/B-VII.1 library	Isotope
No neutron library in MCNP 6.2	^{18}O, ^{108}Ag, ^{158}Tb
No photonuclear library in MCNP 6.2	^{232}Th, ^{233}U, ^{234}U, ^{236}U, ^{238}Pu, ^{241}Pu
No probability table in MCNP 6.2	^{22}Na, ^{36}Ar, ^{58}Co, ^{65}Zn, ^{70}Ge, ^{106}Cd, ^{170}Tm ^{182}W, ^{186}W, ^{203}Ti, ^{232}U, ^{236}Pu, ^{249}Bk, ^{249}Cf, ^{250}Cf

The isotope-wise verification procedure used in this work is described in what follows.

- MCNP 6.2: For the incident photon source problem, a coupled photon/neutron fixed source is simulated within a homogeneous media with unit volume and a unit number density. The composition of the homogeneous problem is a single isotope of interest. Isotropic photon sources, characterized by varying incident mono-energetic energy, are placed at the center of a 100 cm^3 cube, which can be considered as a semi-infinite medium. To ensure that the relative errors of tallies are below 0.5%, 1E+7 particles are simulated. For the electron-induced problem, the 20 and 40 MeV electron sources are isotropically generated at the center of a target defined as a lead–bismuth eutectic (LBE) target sphere with a 0.3 cm diameter. Subsequently, an electron/photon/neutron fixed-source problem is solved within a homogeneous medium and a target.
- SCALE/MAVRIC: For the SCALE/MAVRIC simulation, the neutron and photon spectrum from MCNP are tallied in 278 and 125 groups, respectively. These modified neutron and photon group structures are originated from the existing SCALE 252 neutron and CSEWG 94 photon multigroup structure, expanded to cover energy ranges above 14 MeV with a few additional groups. For the electron-induced problem, the multigroup photon/neutron spectrum from MCNP was fed into MAVRIC using the "read source" block. The fixed source problem with both the photon and neutron sources was solved with SCALE/MAVRIC by processing the input and reading the photoatomic and photonuclear CE library files, resulting in the multigroup photon/neutron flux spectrum tally. Because the photonuclear capability is under development, SCALE/MAVRIC does not produce the neutron creation summary by photonuclear reaction, whereas MCNP provides it. Thus, the photonuclear production rate is approximated by dividing the total neutron flux by the photon flux. This flux is normalized to the photon source obtained from MCNP.

6.1 PHOTON-INDUCED PROBLEM

Figures 20 through 23 present the photon production results for individual isotopes with incident photon energies of 15, 20, 30, and 40 MeV. The photonuclear production rate was approximately estimated by the ratio of photon and neutron flux in the infinite media. Note that this photonuclear production rate includes the absorption of photons and neutrons during transport simulation. The photonuclear production results obtained without the TTB approximation closely matched those obtained by MCNP 6.2. Errors in total photonuclear production for most isotopes were less than 5%, and only a few were greater than 5% (^{2}H, ^{38}Ar, ^{237}Np, ^{239}Pu, ^{240}Pu and ^{241}Am). For ^{2}H, because the medium consists of deuterium only, the small difference in scattering and absorption cross sections between MCNP and SCALE is expected to be exaggerated in the photon and neutron flux estimation in a medium. For ^{237}Np, ^{239}Pu, ^{240}Pu, The error tends to increase with the energy of the incident photon source. This observation of increased error with the rising energy of the incident photon source is consistent with challenges in data extrapolation and modeling for high-energy photonuclear interactions. As mentioned in Section 2, photonuclear data for some nuclides are provided up to a specific upper energy limit (e.g., 20 MeV), whereas most photonuclear data may extend up to 150 MeV. To address discrepancies in the energy range coverage of neutron and photonuclear cross section

data within the ENDF/B-VII.1 database, SCALE libraries were adjusted to ensure consistency across photon and neutron data sets. Regarding nuclides for which photonuclear cross section data are available up to a certain threshold—such as 20 MeV—and for which photonuclear data are available up to 100 MeV, the SCALE libraries were expanded to these higher energy limits. This expansion was achieved by holding the cross section values constant at the last available data point, avoiding any extrapolation beyond this limit. Consequently, this can introduce discrepancies in cross section values when comparing SCALE to MCNP, particularly at high-energy photon regions, in which the bias may become more pronounced. The list of isotopes can be found in Table 2. With respect to ^{241}Am, it was previously pointed out that the difference in photonuclear production arises from the differing fission yield between SCALE and MCNP 6.2 [6]. For ^{38}Ar, further investigation is required to reveal the difference between MCNP and SCALE. Although the errors in neutron production of ^{2}H and ^{38}Ar are not negligible, they are typically less significant in broader photonuclear production applications.

For results applying the TTB model, notable discrepancies in SCALE/MAVRIC simulations were observed for lightweight materials. An overestimation of photonuclear production occurred for these materials and can be attributed to the TTB model's simplified representation of electron and photon cascade at lower photon energies and lack of consideration for electron shell effects. Such simplifications can lead to a relative increase in calculated secondary neutron production due to an over-represented yield from bremsstrahlung interactions. Nevertheless, the results with 30 MeV and 40 MeV from SCALE/MAVRIC align more closely with those from MCNP simulations. The improved correlation at higher energies confirms the model's robustness in scenarios with a high-energy range in which the TTB reactions are more pronounced.

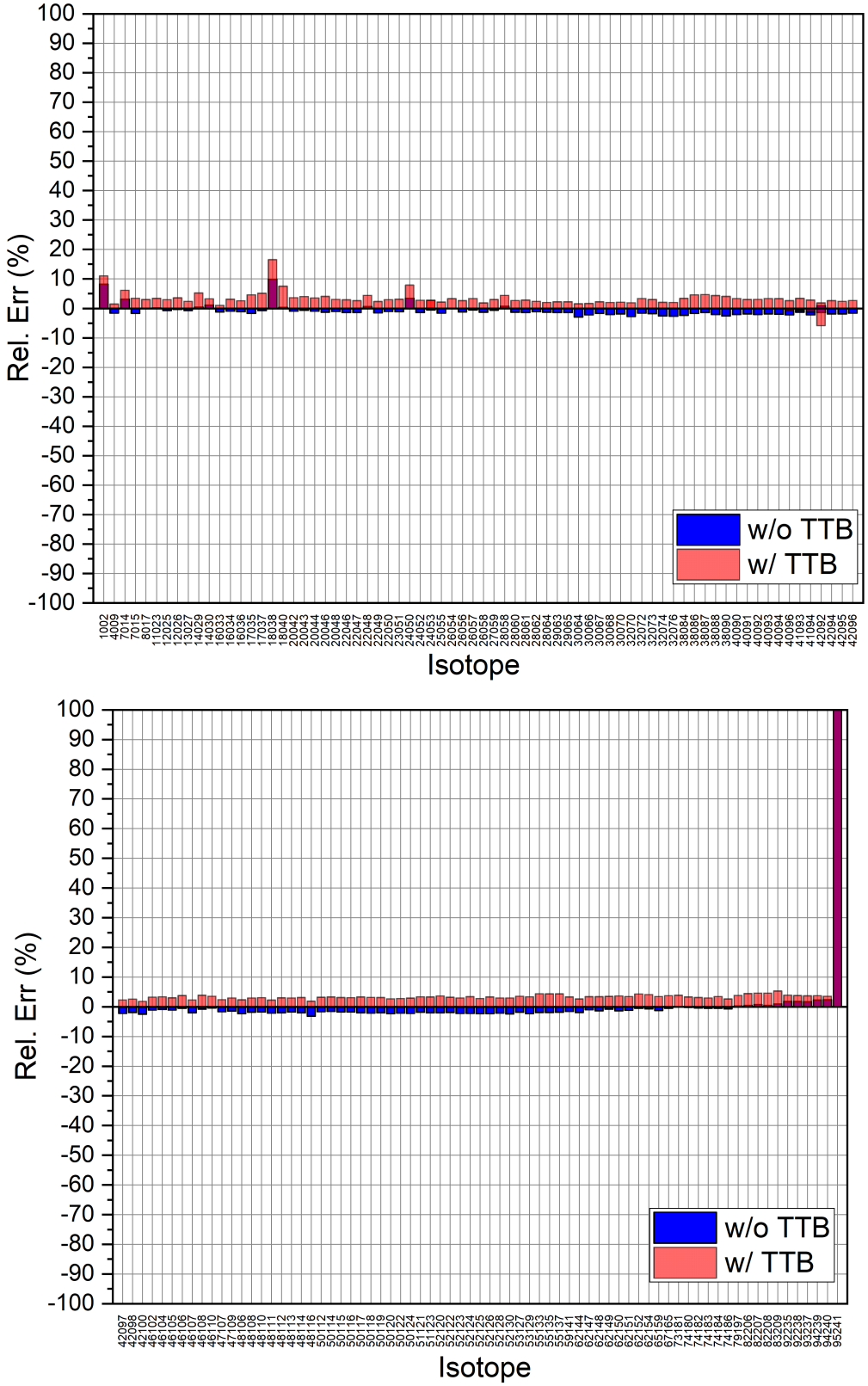

Figure 20. Relative error of photonuclear production with 15 MeV incident photon sources.

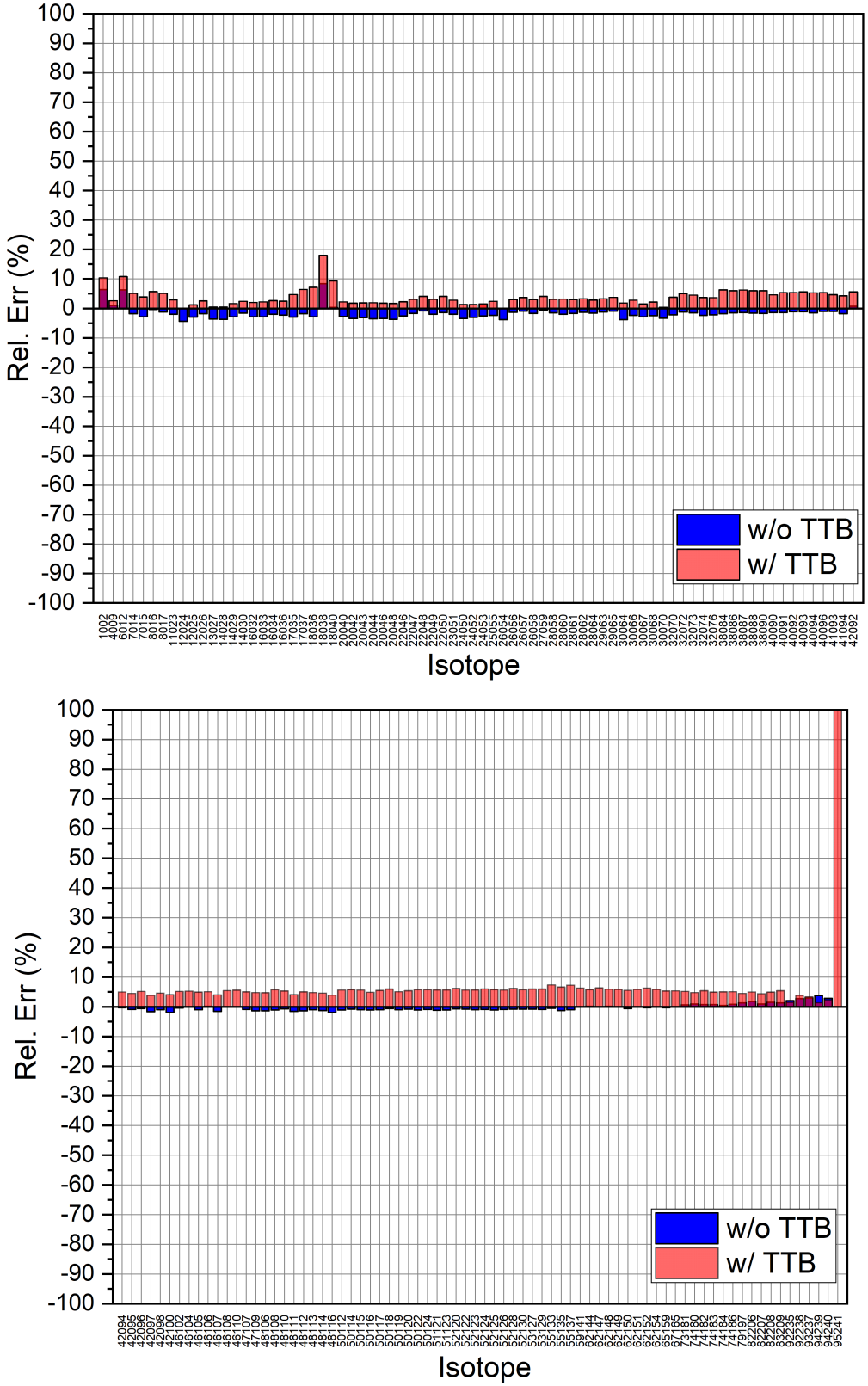

Figure 21. Relative error of photonuclear production with 20 MeV incident photon sources.

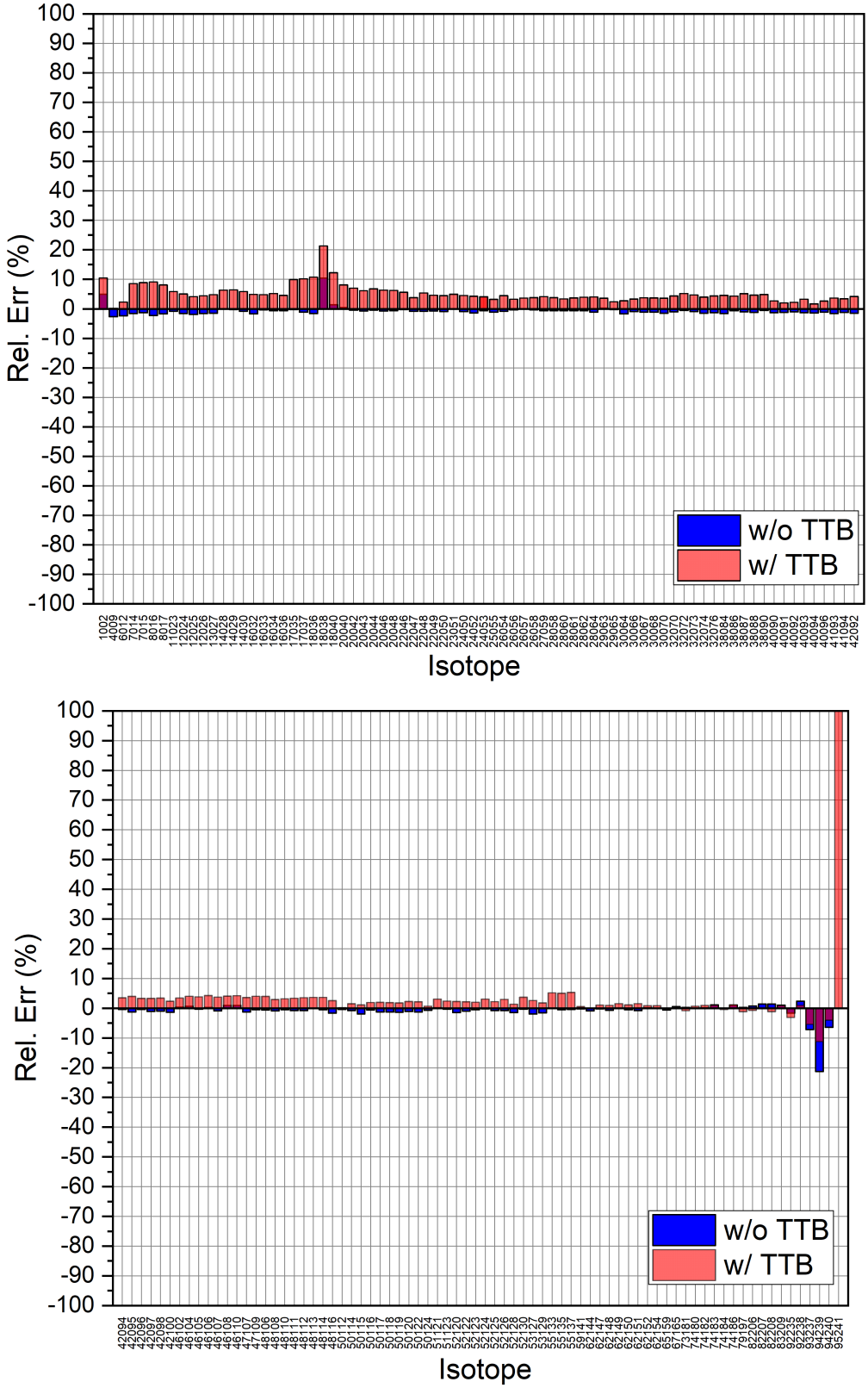

Figure 22. Relative error of photonuclear production with 30 MeV incident photon sources.

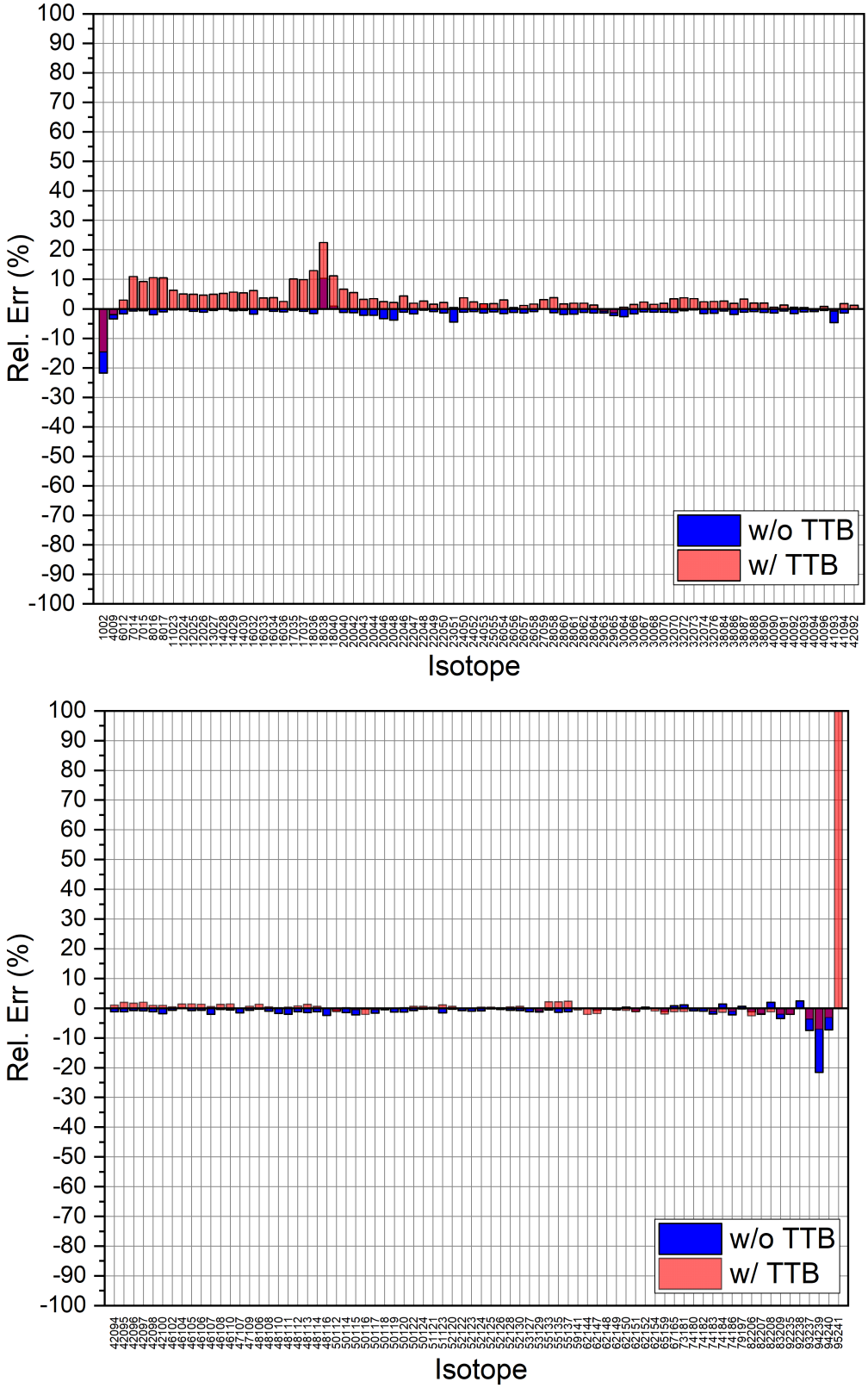

Figure 23. Relative error of photonuclear production with 40 MeV incident photon sources.

Photonuclear production is an integrated value. To ascertain the accuracy of the resulting photon and neutron spectra, a comparison of spectra obtained from MCNP and SCALE/MARIC was performed. This analysis verifies the photon and neutron flux distributions for photon-induced reactions at the energy levels of 20 MeV and 40 MeV. The root mean squared relative error (RMSRE) metric provides a quantitative measure of the deviation between the SCALE/MAVRIC and MCNP-calculated spectra, offering integrated value of multigroup errors for representing photon and neutron transport accuracy in various isotopic compositions and energy. The RMSRE for the spectrum was defined as

$$\textbf{RMSRE} = \sqrt{\frac{1}{G}\sum_{g=1}^{G}|e_g|^2}\text{ , where } e_g = \frac{\phi_{g,scale} - \phi_{g,mcnp}}{\phi_{g,mcnp}} \tag{97}$$

To avoid meaningless large relative error due to the statistical uncertainty for the groups that have very low photon and neutron flux levels, a 0.5% threshold compared to the total flux was established to exclude statistically uncertain data in low-flux groups from the error calculation. SCALE photon flux distribution was normalized to the total photon flux level of MCNP in the RMSRE calculation. Figures 24 through 27 illustrate the RMSRE for the photon and neutron flux distributions across all isotopes. It is worth highlighting in 24 that the RMSREs of SCALE were approximately 5% lower than those from MCNP with and without the TTB approximation for light- and intermediate-weight isotopes. However, notable discrepancies for the heavy isotopes (Z>67) were observed. The observed overestimation of photon flux in the higher energy spectrum can be attributed to different physics enabled in MCNP and SCALE. In this comparison, a detailed photon physics treatment in MCNP was enabled up to 100 MeV. In the MCNP detailed photon physics treatment, photoelectric absorption can result in fluorescent emission, and the Thomson and Klein–Nishina differential cross sections are modified by appropriate form factors [22]. Because SCALE has a different form factor for Thomson and Klein–Nishina differential cross sections and does not simulate fluorescent emissions, the resulting photon spectrum difference was affected. For example, 28 shows the relative normalized photon flux error between MCNP and SCALE. It can be clearly seen from the figure that there is a huge underestimation of photon flux at 0.1 MeV due to the lack of fluorescent emission in SCALE data, which results in the high RMSRE for ^{235}U in 24. 29 shows the RMSRE results compared against MCNP with simplified photon physics treatment, which disables the fluorescent emission. The results demonstrate that the SCALE photon flux agrees well with that of MCNP. However, this photoelectric absorption with fluorescent emission occurs at low energy ranges, and this photon flux difference does not affect the photonuclear reactions. This can be easily understood from the fact that the RMSRE of 25 is generally less than 5% for all isotopes. Because the objective was to verify the photonuclear reaction that occurs generally higher than a few MeV energy ranges, the detailed photon physics treatment was used for the MCNP calculation for the rest of the verification. Similar to the photonuclear production results, the 40 MeV case shows slightly higher RMSRE than the 20 MeV case. This result is due to the difference in data above the energy limit, as described above, as well as the aforementioned difference in Thomson and Klein–Nishina differential cross sections form factor between MCNP and SCALE.

Consequently, this verification supports the use of the SCALE/MAVRIC suite with its photonuclear library as a reliable tool for accurately simulating photon-induced nuclear reactions across a broad energy spectrum, enhancing its comparability to established codes such as MCNP 6.2 for a range of applications in nuclear engineering.

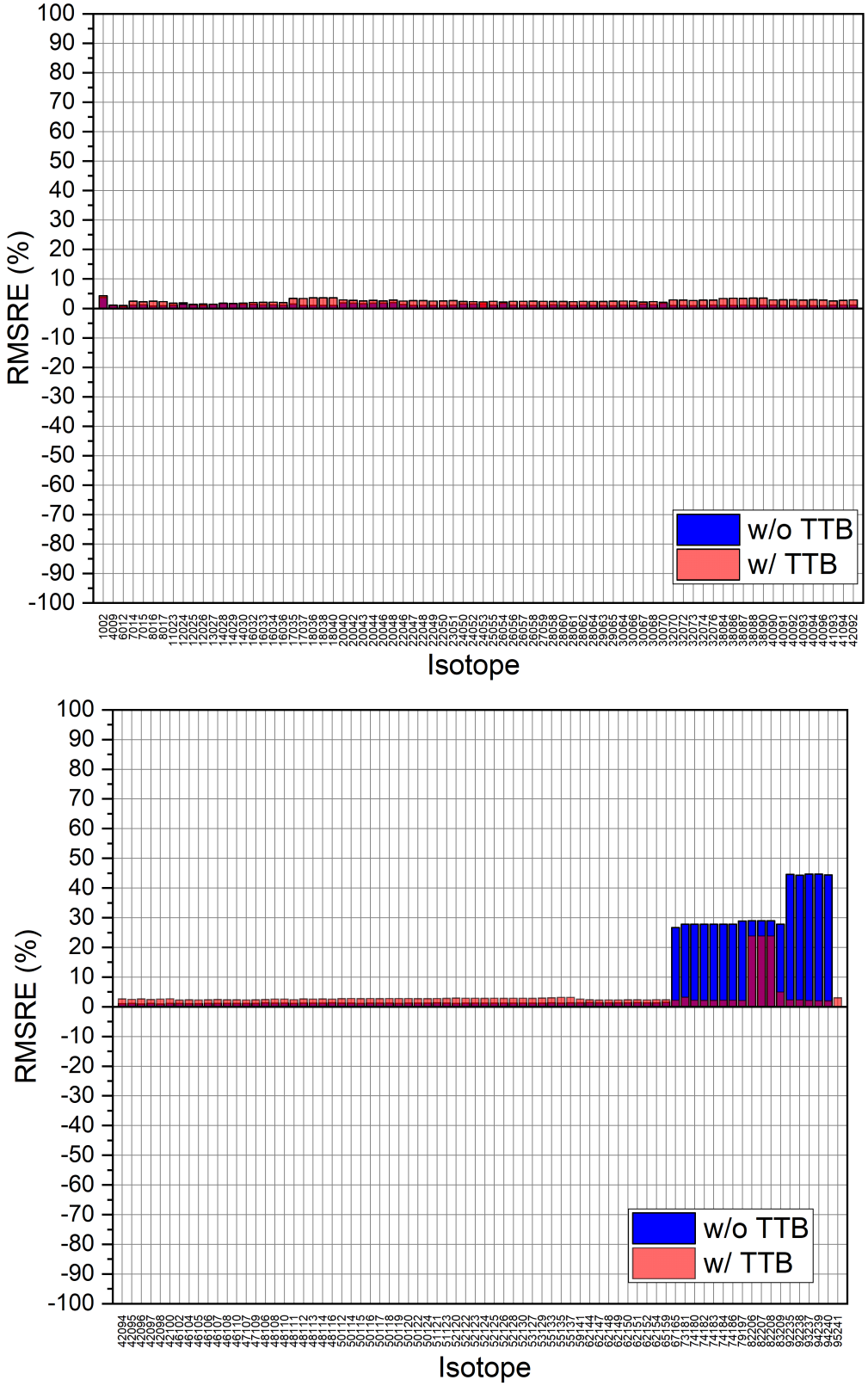

Figure 24. RMSRE of photon flux distribution with 20 MeV incident photon sources.

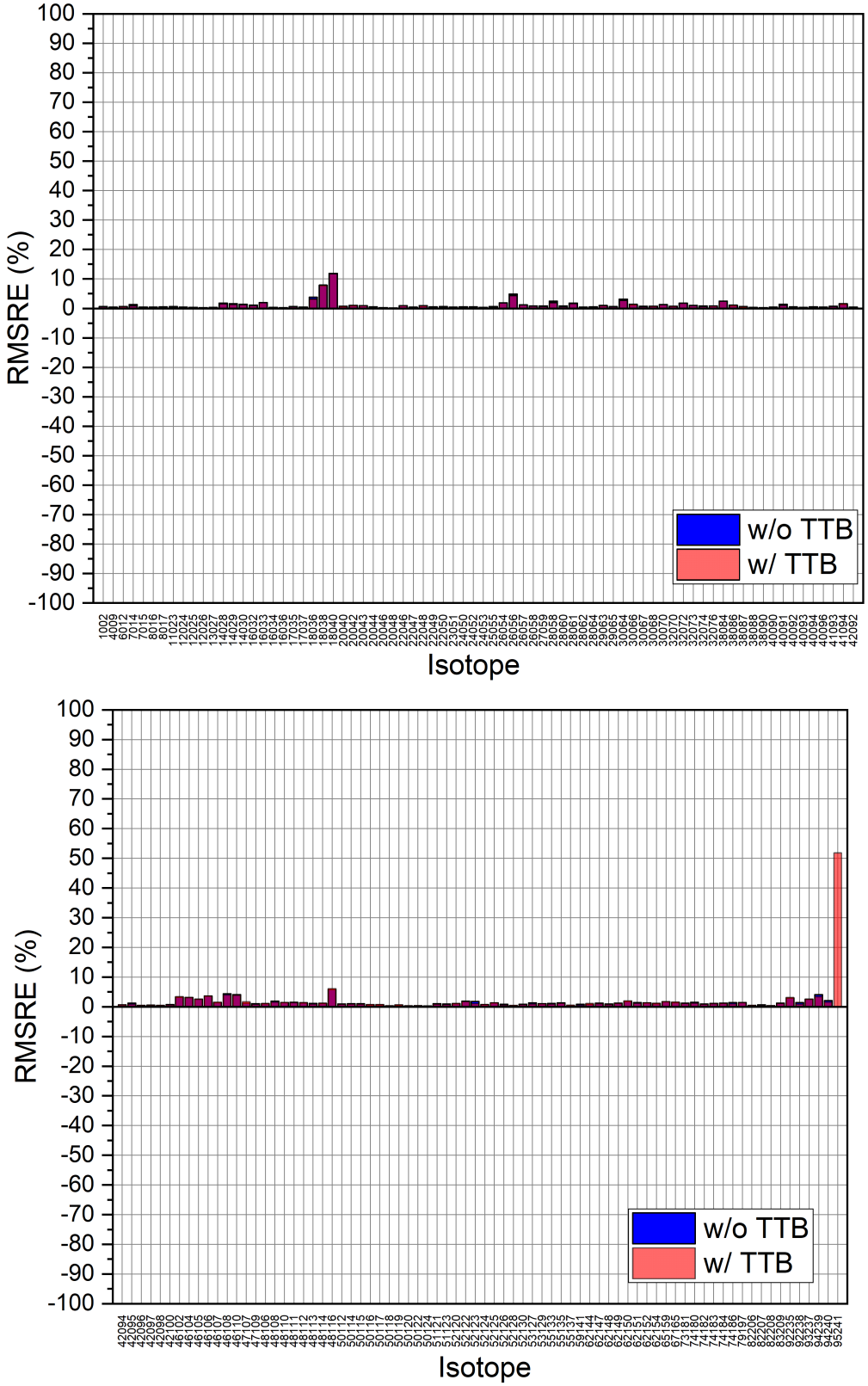

Figure 25. RMSRE of neutron flux distribution with 20 MeV incident photon sources.

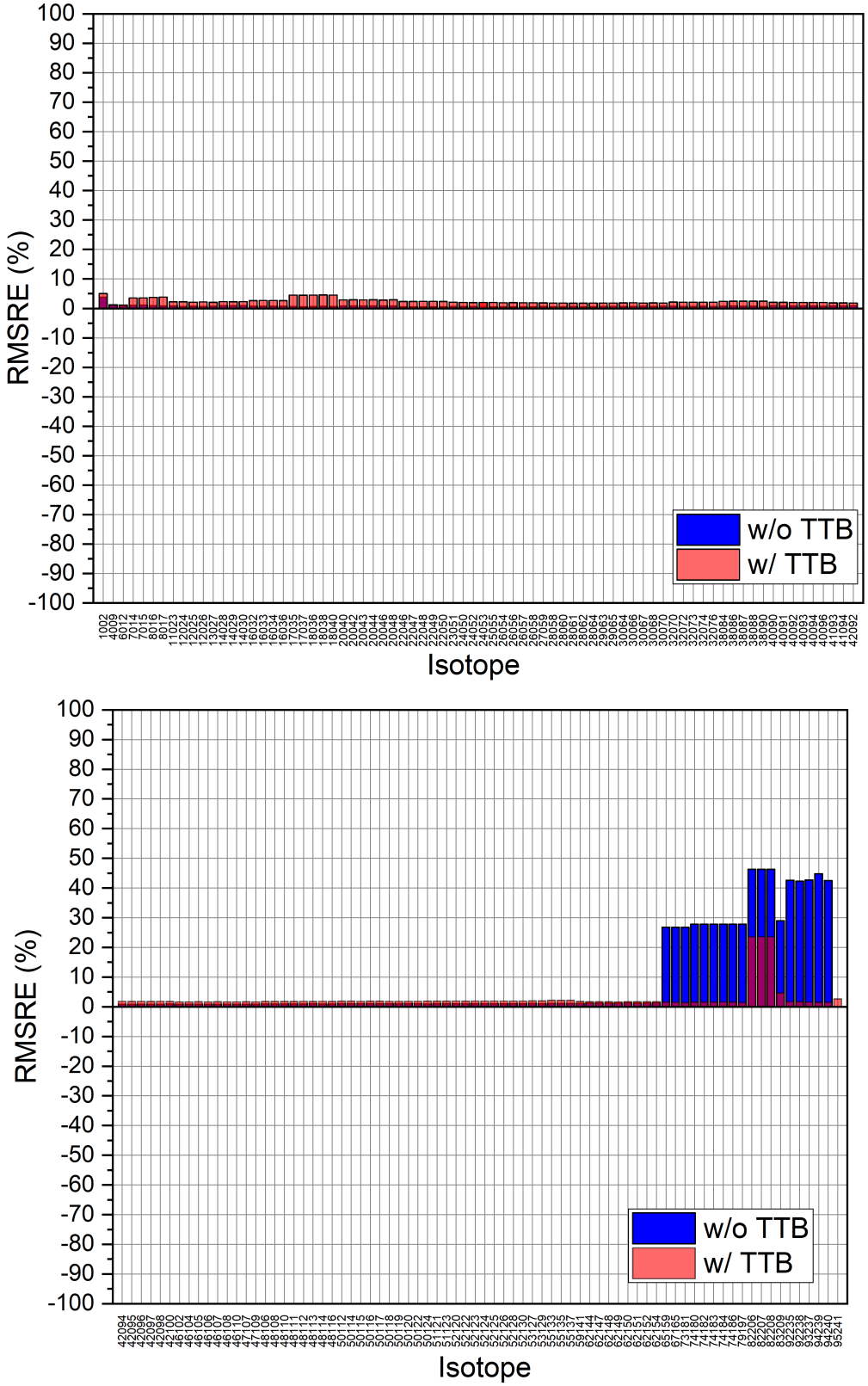

Figure 26. RMSRE of photon flux distribution with 40 MeV incident photon sources.

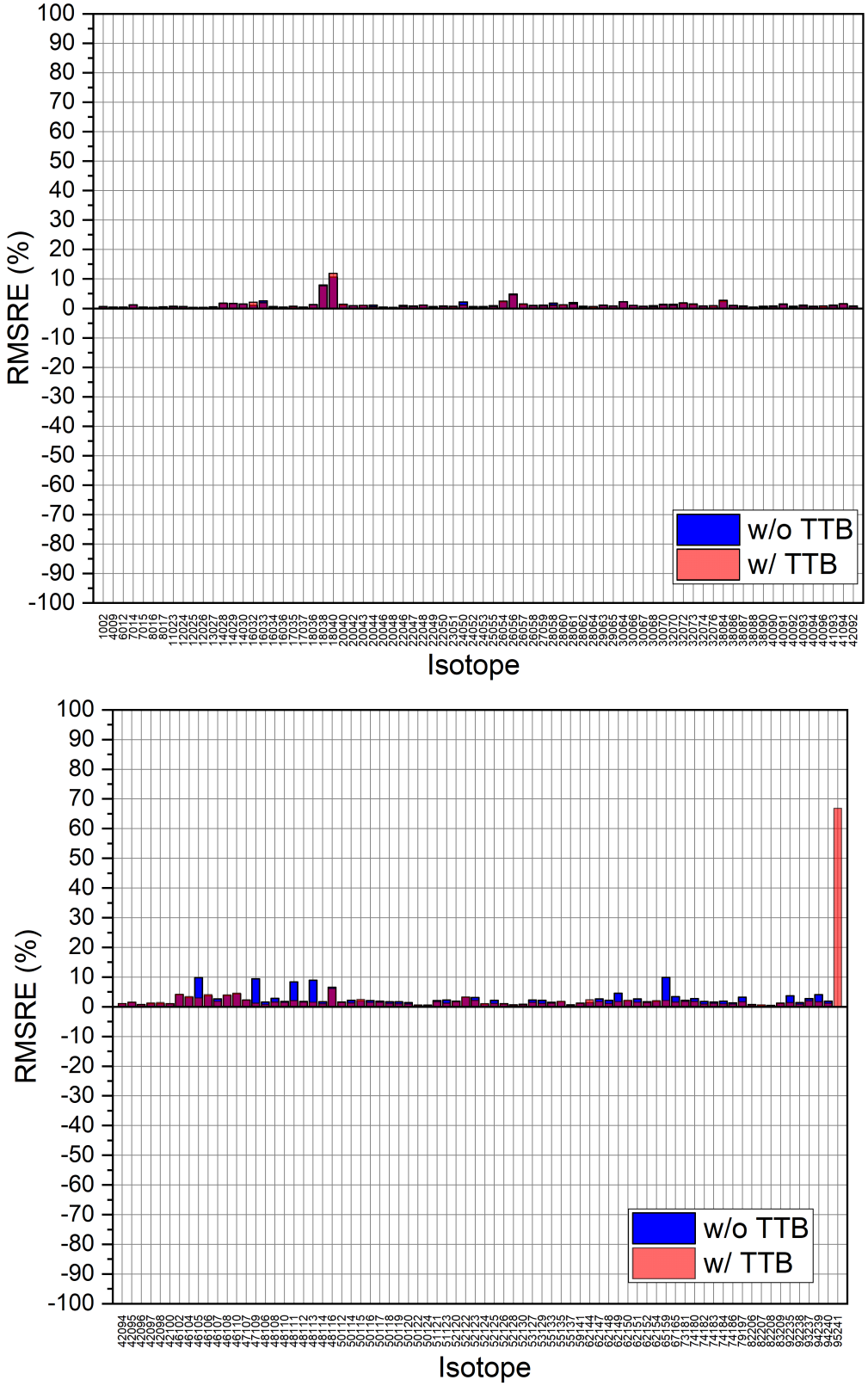

Figure 27. RMSRE of neutron flux distribution with 40 MeV incident photon sources.

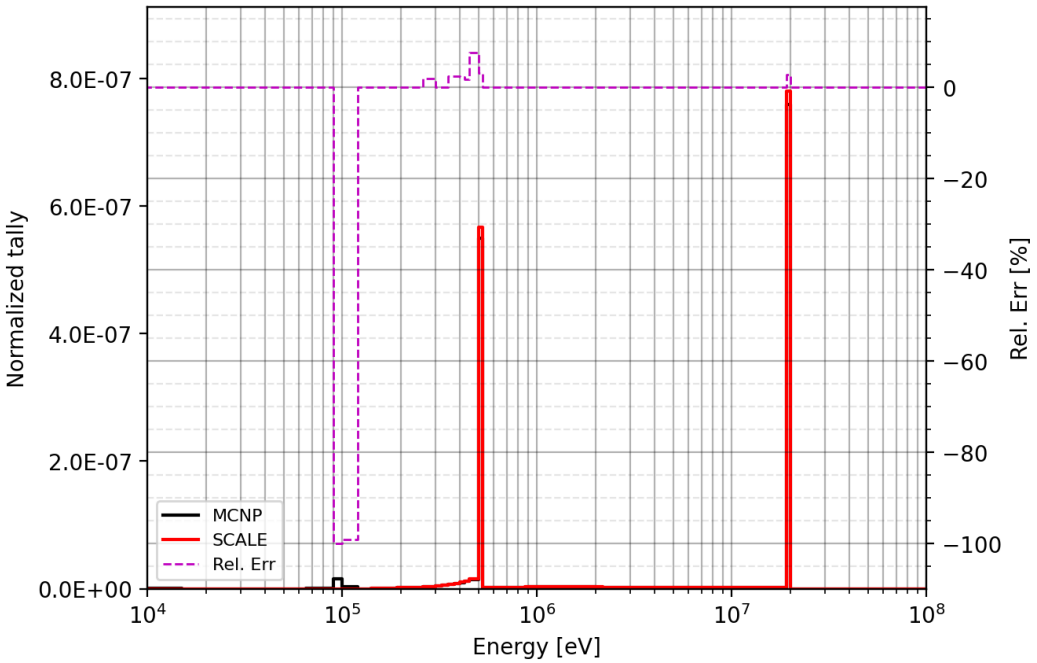

Figure 28. Relative error of multigroup photon flux distribution with 20 MeV incident photon sources for ^{235}U.

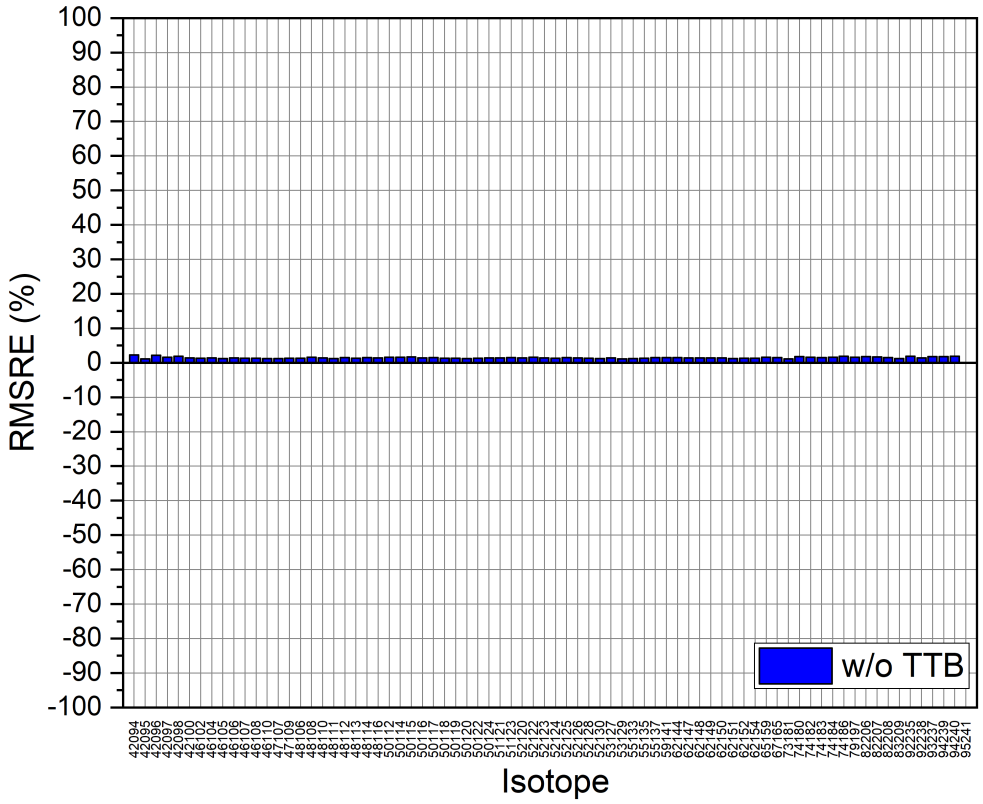

Figure 29. RMSRE of photon flux distribution with 20 MeV incident photon sources (simplified photon physics in MCNP.

6.2 ELECTRON-INDUCED PROBLEM

When compared to the MCNP 6.2 results, the photon-induced problem results from this work prove that the newly developed photonuclear library and transport capability in SCALE work well. The verification was extended to the electron-induced problem in this section to test the applicability of the MCNP/SCALE hybrid approach in the ^{99}Mo production. The purpose of an electron-induced problem test is to estimate the photonuclear production rates in a semi-infinite homogeneous media for each isotope with a small target in the center. Because the goal of the work documented in this report was to accurately estimate the ^{99}Mo production rates in a UO_2 assembly with the high-energy electron source used in the ^{99}Mo program collaborator's facility using hybrid MCNP/SCALE simulation, the LBE was selected as a target material for future application [2].

The verification was conducted with the isotropic electron sphere sources at the center. The photon and neutron leakage outside the target tallied from MCNP were given as isotropic sources at the center of the target in the SCALE simulation. This methodology presents challenges as target dimensions increase because of the backscattering of radiation into the LBE from the surrounding medium, potentially leading to an underestimation of photonuclear yield in the tallied region. In this case, there will be additional absorptions of back-scattered photon or neutron in the target, leading to the underestimation of photonuclear production in the tally region. If the target is small enough compared to the semi-infinite media size, then these target approximations are valid. However, if the target is too small compared to the radiation length of the target, then significant electron leakage outside of the target will occur that cannot be simulated in SCALE. Thus, for these verification tests, care was taken in the determination of the adequate target size for the MCNP electron simulation to minimize the leakage of electrons outside of the target and to minimize the back-scattered photon/neutron source. The size of the LBE target was determined to be a 0.25 cm sphere to minimize the electron leakage outside of the tally region by less than 0.1% as well as to minimize the back-scattered photon/neutron current level compared to the photon/neutron flux levels. The tallied photon and neutron spectrum from MCNP was normalized to the initial photon source level of MCNP.

In Figures 30 to 31, the outcomes for photonuclear reactions using 20 and 40 MeV electron sources are shown. The results from SCALE, when compared to MCNP 6.2 in Figure 30, mostly match except ^{126}Te, ^{206}Pb, ^{207}Pb and ^{208}Pb, but a slight increase in error was generally observed compared to the photon-induced problems. The cause of this discrepancy lies in the way SCALE treats the source of photons and neutrons from MCNP. As shown in Figure 28, there is a huge photon source peak in the vicinity of the incident photon energy. In the electron-induced problem, a similar photon source peak was observed at the incident electron energy. In addition, photons undergo slowing down from the source, and thus the flux distribution increases within a group. This distribution was tallied in multigroup format and distributed uniformly within the coarse group structure for the SCALE input. This results in the underestimation of photonuclear production due to the softened photon spectrum. For ^{206}Pb, ^{207}Pb and ^{208}Pb, the error can be attributed to different physics, fluorescent emission, between SCALE and MCNP as described in the photon-induced problem. For ^{126}Te, further investigation is required to reveal the difference between MCNP and SCALE especially for the TTB approximation at higher energy range. The discrepancy of ^{241}Am noted in the photon-induced problem, attributed to the absence of photon fission yield data in the MCNP library, was not observed in the electron-induced problem. This variation can be ascribed to the differences in the photon flux spectra between the two types of sources. In the electron-induced problem, the photon flux spectrum is more softened, lacking the pronounced photon peak at the incident energy of photon-induced problems. Note that the photon-fission reaction for ^{241}Am typically occurs at an energy range above a few MeV. The softened spectrum in electron-induced cases thus has almost zero photo-fission reactions, which could explain the absence of the error seen in the photon-induced problem.

Figures 32 through 35 show the RMSRE for the photon and neutron flux distributions for electron-induced problems. The comparisons reveal a uniform source modeling assumption in SCALE that leads to some

inaccuracies in photon estimations; this inaccuracy is evident in the deviations observed between MCNP and SCALE simulations. However, the neutron predictions align well. To enhance accuracy, MCNP and SCALE should incorporate more detailed energy grouping or account for the within-group distribution of photon sources based on the MCNP tally information. The current approach uses broad energy categories to accommodate a range of incident energy sources, which may not be sufficiently precise for some applications. Nevertheless, even with these broader groupings, the hybrid MCNP/SCALE method achieves verification with less than a 5% error in the photonuclear production rate.

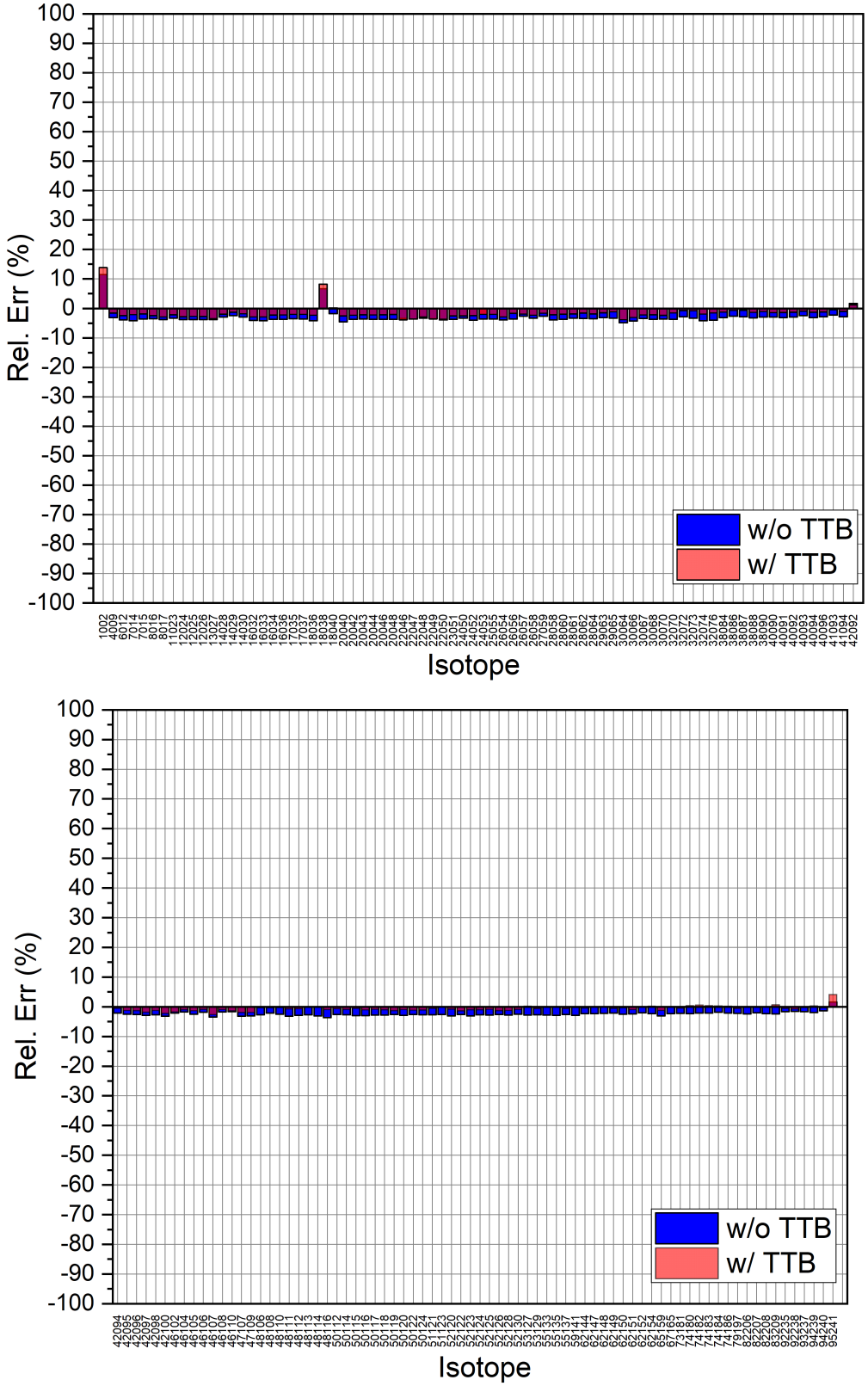

Figure 30. Relative error of photonuclear production with 20 MeV incident electron sources.

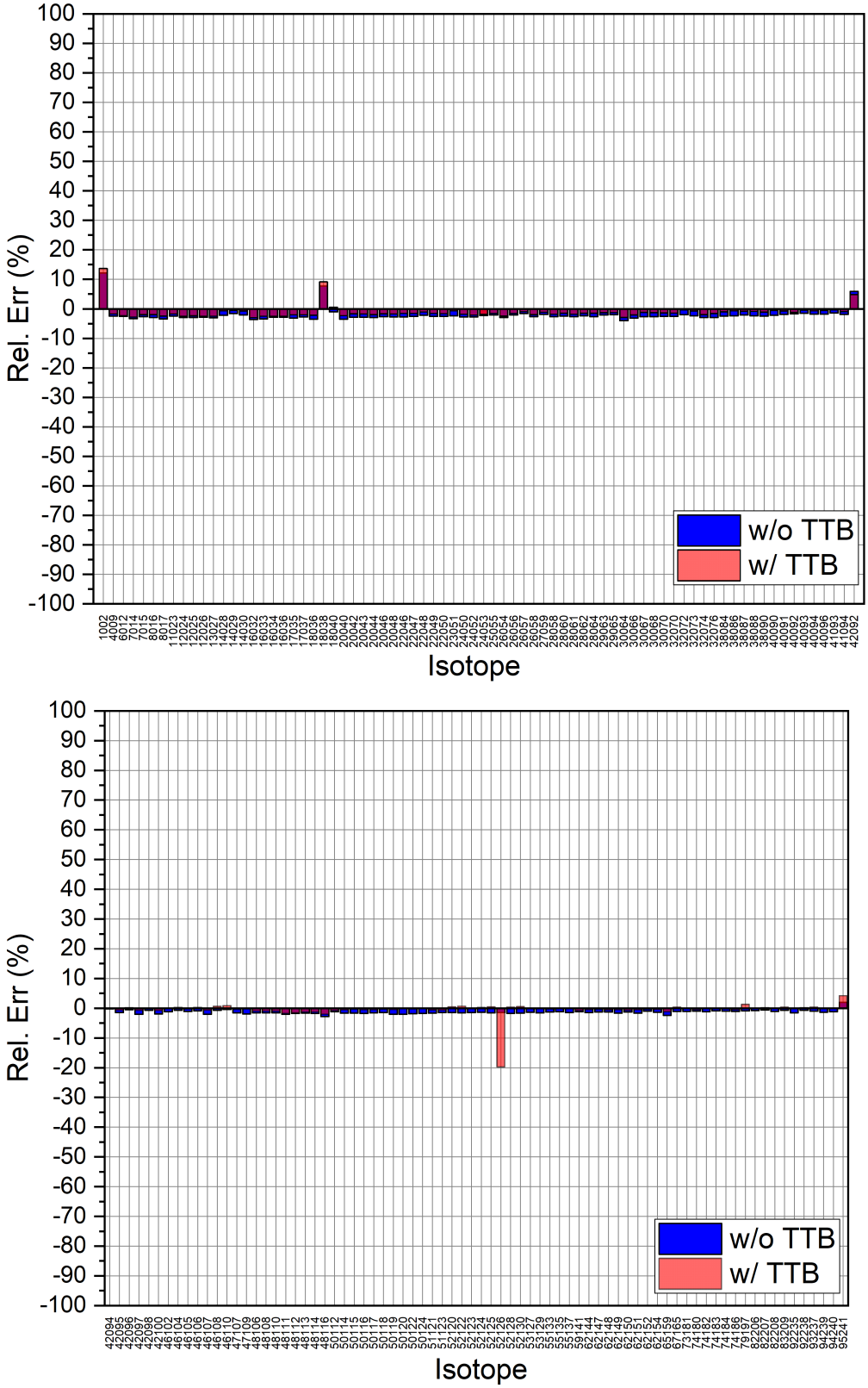

Figure 31. Relative error of photonuclear production with 40 MeV incident electron sources.

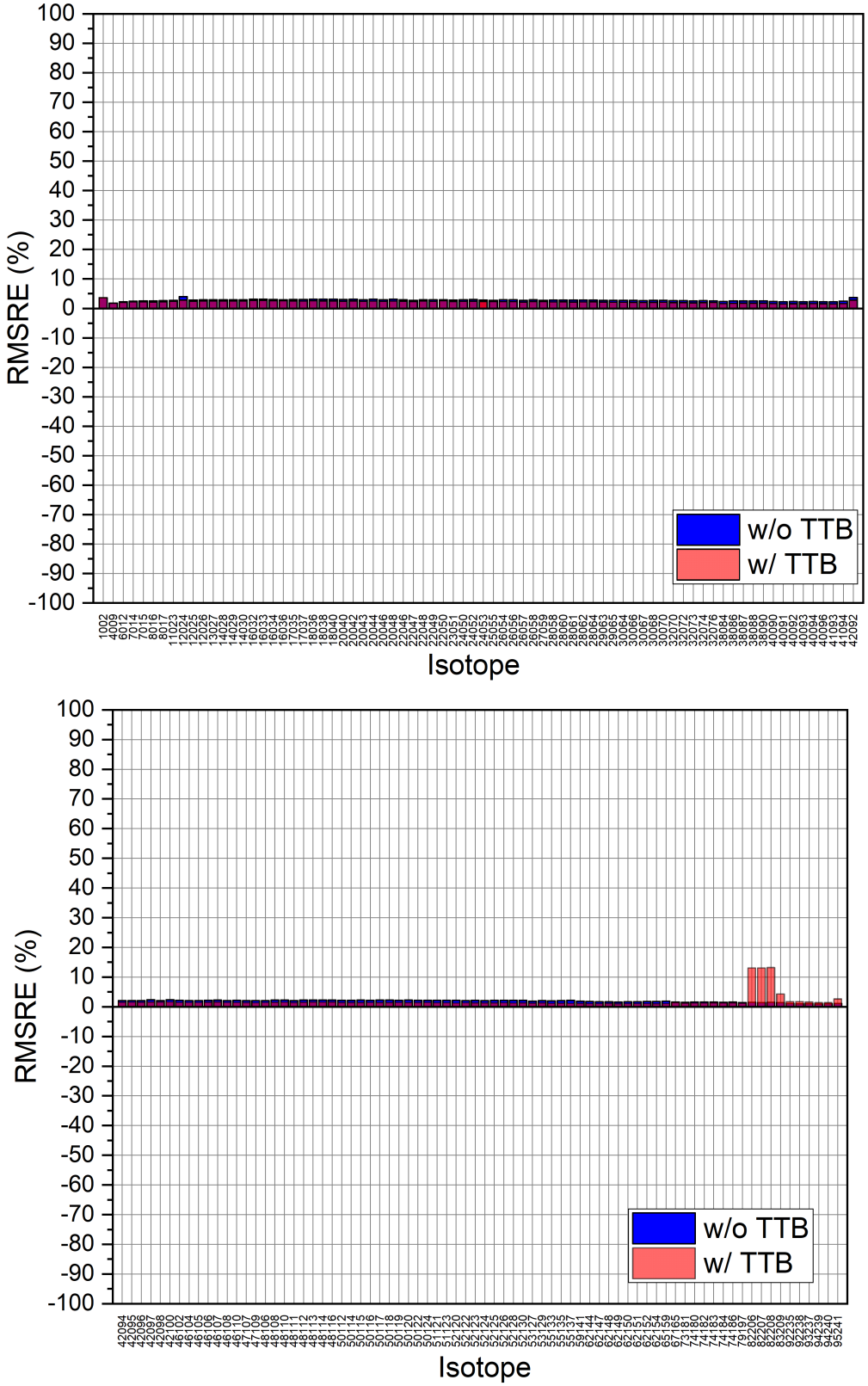

Figure 32. RMSRE of photon flux distribution with 20 MeV incident electron sources.

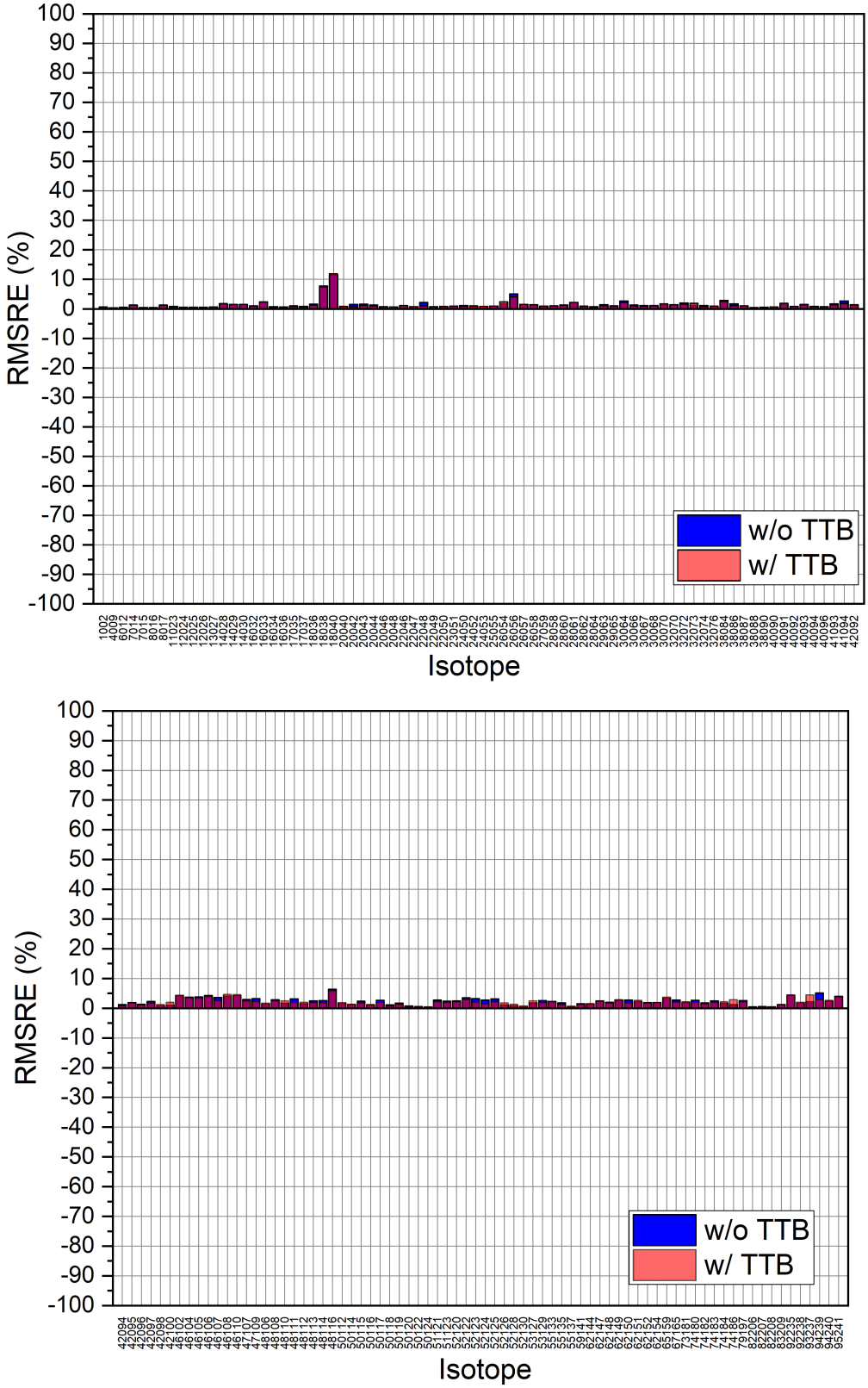

Figure 33. RMSRE of neutron flux distribution with 20 MeV incident electron sources.

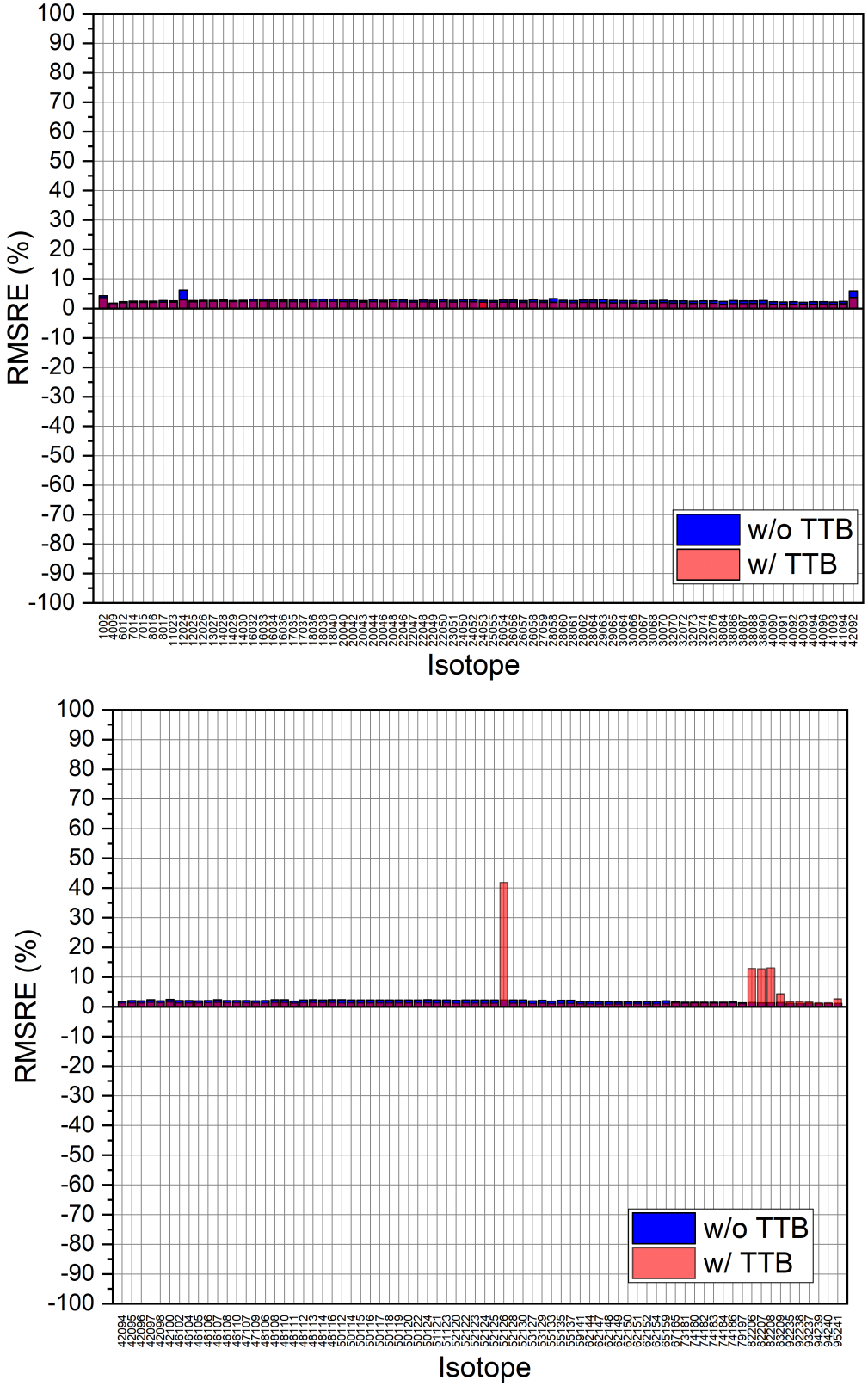

Figure 34. RMSRE of photon flux distribution with 40 MeV incident electron sources.

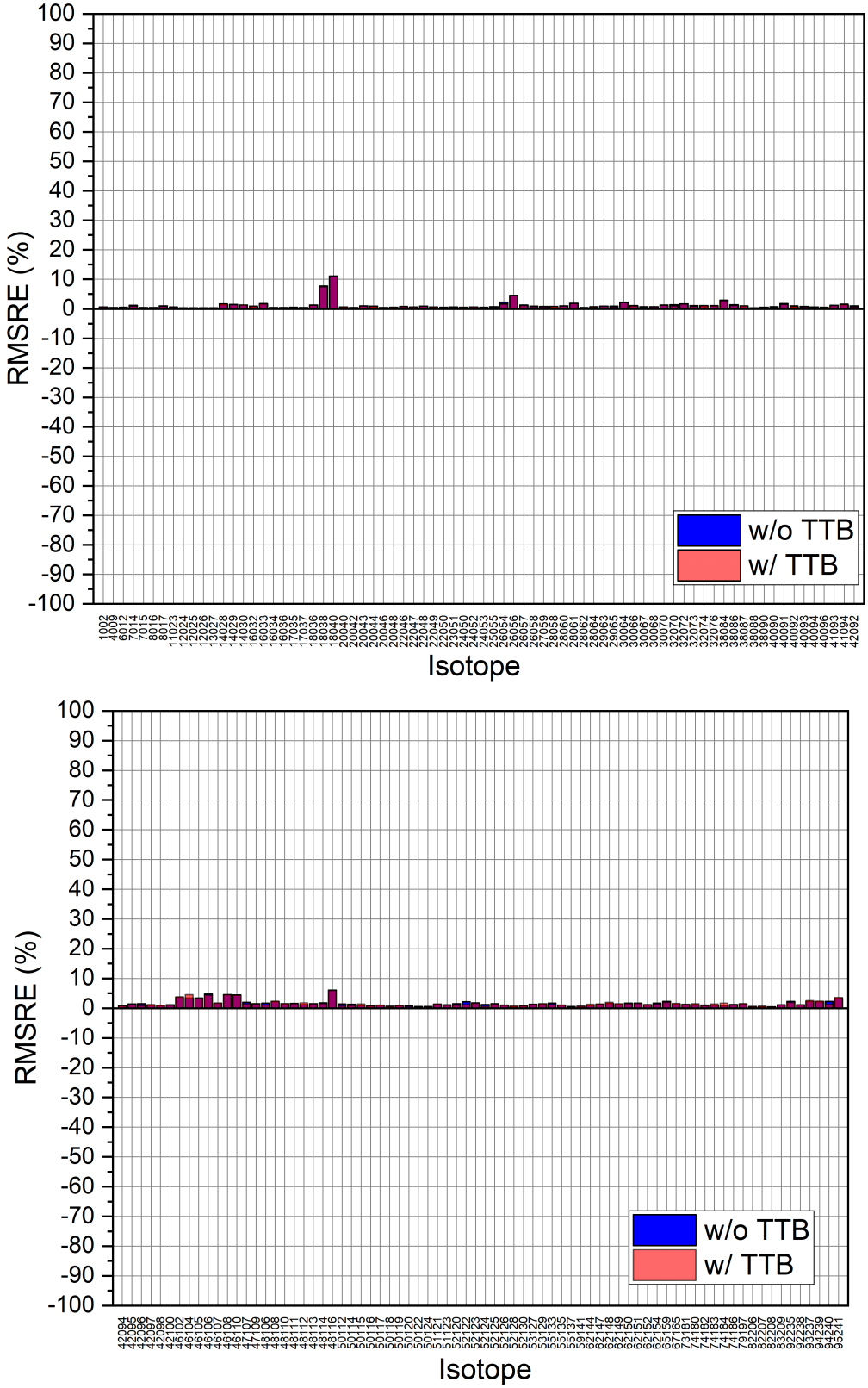

Figure 35. RMSRE of neutron flux distribution with 40 MeV incident electron sources.

7. CONCLUSION

In conclusion, this report has comprehensively evaluated the photonuclear simulation capabilities in SCALE/MAVRIC, benchmarking its performance against MCNP 6.2. Key components of the study included the adaptation of the ENDF/B VII.1 photonuclear library for both SCALE/MAVRIC and MCNP simulations and the implementation of photonuclear reaction in photon simulation in SCALE/MAVRIC for photonuclear yield estimations. The report also showcased the ability of hybrid MCNP/SCALE to effectively estimate neutron and photon production rates and their flux distributions with various target materials, compensating for its intrinsic limitations in the lack of electron transport simulation in SCALE. Furthermore, the study highlighted the significance of accurately modeling the Bremsstrahlung reactions with high-energy electrons and photons to capture the electron-photon cascade that affects the photonuclear production rates. To model this explicitly, the TTB model was developed and implemented in SCALE/MAVRIC. Overall, the findings demonstrate the robustness and reliability of the SCALE/MAVRIC in simulating photonuclear reactions, having less than 5% relative errors of photonuclear production rates and flux distribution for most isotopes with sources of various energy and particle types.

8. FUTURE WORK

One of the goals for ongoing work in this project is to complete the implementation of the multigroup photonuclear physics. A preliminary multigroup library with 31 neutron groups and 23 photon groups has been prepared. This library needs to be coupled with necessary updates to the multigroup physics in MAVRIC, followed by thorough testing and validation. It will also be coupled to work in Denovo for accelerated variance reduction. Another future work is to have a fine multigroup library with photonuclear reactions to be used in the radiation shielding analyses. A more detailed physics to represent the Bremsstrahlung electron and positron interaction can be achieved by accounting for the particle transport of electrons and positrons. Facility shielding optimization requires variance reduction methods working in tandem with particle transport simulations and ensuring MAVRIC coupled-physics particle transport simulations with CADIS and FW-CADIS methods will be a high priority in the future.

REFERENCES

[1] E. W. A. Wieselquist R. A. Lefebvre, "SCALE 6.3.1 User Manual," Oak Ridge National Laboratory, Oak Ridge, Tennessee, Technical Report ORNL/TM-SCALE-6.3.1, 2023.

[2] N. B. Nelson, M. B. R. Smith, Z. Karriem, J. Navarro, C. P. Denbrock, R. N. Wahlen, *et al.*, "Radiation Shielding Analysis of Niowave's Uranium Target Assembly 2 (UTA-2) Facility for Molybdenum-99 Production," Oak Ridge National Laboratory, Oak Ridge, TN, Tech. Rep. ORNL/TM-2021/2269, Jul. 2022. DOI: 10.2172/187871. [Online]. Available: https://www.osti.gov/biblio/1878714.

[3] D. Wiarda, M. E. Dunn, N. M. Greene, M. L. Williams, C. Celik, and L. M. Petrie, "AMPX-6: A Modular Code System for Processing ENDF/B," Oak Ridge National Lab (ORNL), Oak Ridge, TN (United States), Tech. Rep. ORNL/TM-2016/43, Apr. 2016.

[4] M. B. Chadwick, P. Obložinský, M. Herman, N. M. Greene, R. D. McKnight, D. L. Smith, *et al.*, "ENDF/B-VII.0: Next Generation Evaluated Nuclear Data Library for Nuclear Science and Technology," *Nuclear Data Sheets*, Evaluated Nuclear Data File ENDF/B-VII.0, vol. 107, no. 12, pp. 2931–3060, Dec. 2006. DOI: 10.1016/j.nds.2006.11.001. [Online]. Available: https://www.sciencedirect.com/science/article/pii/S0090375206000871.

[5] A. Trkov, M. Herman, and D. A. Brown, "ENDF-6 Formats Manual," Brookhaven National Lab. (BNL), Upton, NY (United States), Tech. Rep. BNL-203218-2018-INRE, 2018. [Online]. Available: https://www.nndc.bnl.gov/endf/b8.0/endf-manual-viii.0.pdf.

[6] *Photonuclear ACE file processing does not handle MF5 LF=5, 11 or 12*, https://github.com/njoy/NJOY2016/issues/269, Accessed: 2023-10-06.

[7] F. Salvat, "PENELOPE-2014: A Code System for Monte Carlo Simulation of Electron and Photon Transport," OECD Nuclear Energy Agency, Barcelona, SP, Tech. Rep. NEA/NSC/DOC(2015)3, Jul. 2015.

[8] F. Salvat and J. M. Fernández-Varea, "Overview of physical interaction models for photon and electron transport used in Monte Carlo codes," *Metrologia*, vol. 46, no. 2, S112–S138, Apr. 2009. DOI: 10.1088/0026-1394/46/2/S08. [Online]. Available: http://stacks.iop.org/0026-1394/46/i=2/a=S08?key=crossref.13b06a27bdc9ea580c8b74053fe31b91 (visited on 10/06/2017).

[9] T. Kaltiaisenaho, "Implementing a photon physics model in Serpent 2," Ph.D. dissertation, Aalto University, Finland, 2016.

[10] R. D. Deslattes, E. G. Kessler, P. Indelicato, L. de Billy, E. Lindroth, and J. Anton, "X-ray transition energies: New approach to a comprehensive evaluation," *Rev. Mod. Phys.*, vol. 75, pp. 36–99, 2003.

[11] S. T. Perkins, D. E. Cullen, M. H. Chen, J. H. Hubbell, J. Rathkopf, and J. Scofield, "Tables and Graphs of Atomic Subshell and Relaxation Data Derived from the LLNL Evaluated Atomic Data Library (EADL), Z = 1-100," Lawrence Livermore National Laboratory, Technical Report UCRL—ID-50400, 1991.

[12] S. M. Seltzer and M. J. Berger, "Evaluation of the collision stopping power of elements and compounds for electrons and positrons," *The International Journal of Applied Radiation and Isotopes*, vol. 33, no. 11, pp. 1189–1218, 1982.

[13] T. Carlson, *Photon and Auger Spectroscopy*. New York, NY: Plenum Press, 175.

[14] F. Attix, *Introduction to radiological physics and radiation dosimetry*. New York, NY: John Wiley & Sons, Inc., 1986.

[15] S. Seltzer, "Monte Carlo Transport of Electrons and Photons," in, T. Jenkins, W. Nelson, and A. Rindi, Eds., ser. Ettore Majorana International Science Series. U.S.: Springer, 1988, vol. 38, ch. 4.

[16] S. Seltzer and M. Berger, "Bremsstrahlung energy spectra from electrons with kinetic energy 1 keV - 10 GeV incident on screened nuclei and orbital electrons of neutral atoms with Z=1,100," *Atomic Data and Nuclear Data Tables*, vol. 35, no. 3, pp. 345–418, 1986.

[17] *estar: Stopping-power and range tables for electrons*, 2023. [Online]. Available: https://physics.nist.gov/PhysRefData/Star/Text/ESTAR.html.

[18] R. M. Sternheimer, S. M. Seltzer, and M. J. Berger, "Density effect for the ionization loss of charged particles in various substances," *Physical Review B*, vol. 26, no. 11, 1982. DOI: 10.1103/PhysRevB.26.6067.

[19] D. E. Peplow, "Monte carlo shielding analysis capabilities with mavric," *Nuclear Technology*, vol. 174, no. 2, pp. 289–313, 2011.

[20] D. E. Peplow, S. W. Mosher, and T. M. Evans, "Cmonte carlo shielding analysis capabilities with mavric," Oak Ridge National Laboratory, Oak Ridge, Tennessee, Tech. Rep. ORNL/TM-2012/7, 2012.

[21] J. C. W. E. D. Blakeman and D. E. Peplow, "Forward-weighted cadis method for global variance reduction," *Transactions of the American Nuclear Society*, vol. 97, pp. 630–633, 2007.

[22] C. J. Werner, J. C. Armstrong, F. B. Brown, J. S. Bull, L. Casswell, L. J. Cox, *et al.*, "MCNP User's Manual Code Version 6.2," Los Alamos National Laboratory, Los Alamos, NM, USA, Tech. Rep. LA-UR-17-29981, Oct. 2017.

[23] W. H. Press, S. A. Teukolsky, W. T. Vetterling, and B. P. Flannery, *Numerical Recipes in C*, 2nd, Ed. Cambridge University Press, 1992.

APPENDIX A. WALKER ALIAS SAMPLING METHOD

APPENDIX A. WALKER ALIAS SAMPLING METHOD

Salvat [7] describes the Walker alias sampling method, and it is visualized in Fig. 36. Consider a discrete PDF $p = [0.125, 0.25, 0.075, 0.2, 0.35]$ and $N = 5$. If we define $Np = [0.625, 1.25, 0.375, 1., 1.75]$, then we can make a unit square consisting of columns of width $1/N$. First, sort Np, then define $\delta = 1 - Np_{\mathrm{lo}}$ and add it to Np_{lo} and subtract from Np_{hi}. Iterating in this fashion will yield a square with two probability bins in each column and will converge in at most $N - 1$ iterations. Construction of the unit square requires up to

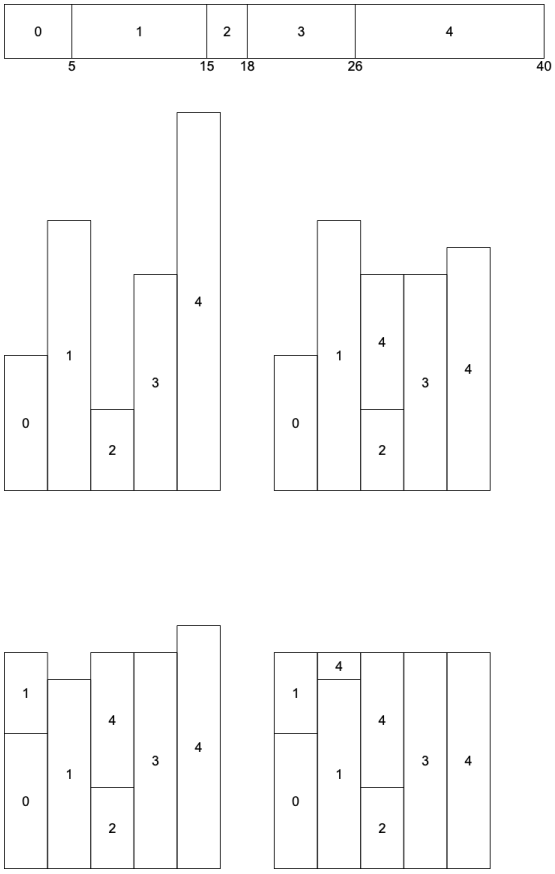

Figure 36. Construction of Walker alias sampling table.

$N - 1$ iterations, each of which requires $O(N \log N)$ sort operations, yielding a total complexity of $(N^2 \log N)$, where N is the size of the PDF. An example of the construction algorithm (using tail recursion) is given in Listing 2.

To sample the bin in the original requires two random numbers (ξ_1, ξ_2), which give the position in the unit square and can be used to determine the probability with two $O(1)$ lookups. However, there is a simplification that requires only a single random number evaluation [7]. If we lay out the unit square linearly as shown in Fig. 37, then we can use the following procedure to sample the bin:

- Sample $\xi \in [0, N]$;
- Find coarse bin (unit-square column) $i = \lfloor \xi \rfloor$;
- Calculate $r = \xi - i$;
- If $r <$ prob$[i]$ return bin$[i, 0]$; otherwise return bin$[i, 1]$.

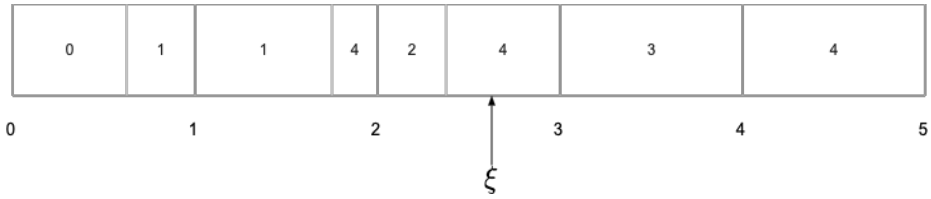

Figure 37. Sampling the unit square with a single random variate.

Listing 2 Python algorithm to construct Walker Alias sampling squares.

```
# Normalize discrete pdf
p = pdf / np.sum(pdf)

# Build the squares
N = pdf.shape[0]
bin = np.zeros((N, 2), dtype='int')
prob = np.zeros((N, 2), dtype='double')

bin[:, 0] = np.arange(N)
bin[:, 1] = -1
prob[:, 0] = p*N
prob[:, 1] = -1.0

_ = build_squares(p*N, 0)

def build_squares(pdf, n):
    if np.allclose(pdf, np.ones(pdf.shape)):
        return pdf

    n += 1
    if n > N - 1:
        raise RuntimeError(
            'Iterations {} > {} (N-1)\n{}'.format(n, N-1, pdf))

    i = np.argsort(pdf)
    d = 1.0 - pdf[i[0]]
    pdf[i[-1]] -= d
    pdf[i[0]] += d

    prob[i[0], 1] = d
    prob[i[-1], 0] -= d

    bin[i[0], 1] = i[-1]

    # Tail recursion
    return build_squares(pdf, n)
```

APPENDIX B. NUMERICAL INTEGRATION SCHEMES

APPENDIX B. NUMERICAL INTEGRATION SCHEMES

B.1 CUBIC SPLINE INTEGRATION

The cubic spline equation is (see Press *et al.* [23], Section 3.3)

$$y = Ay_j + By_{j+1} + Cy''_j + Dy''_{j+1} \,. \tag{B.1}$$

Here,

$$\begin{aligned} A &= \tfrac{x_{j+1}-x}{x_{j+1}-x_j} \,, \\ B &= \tfrac{x-x_j}{x_{j+1}-x_j} \,, \\ C &= \tfrac{1}{6}(A^3 - A)(x_{j+1} - x_j)^2 \,, \\ D &= \tfrac{1}{6}(B^3 - B)(x_{j+1} - x_j)^2 \,. \end{aligned} \tag{B.2}$$

The spline is created on construction from a set of (x, y) values. Then, a set of y can be interpolated at x'. Additionally, it is straightforward to integrate using the equation above because each bin (x_j, x_{j+1}) can be integrated analytically:

$$\int_a^b y(x)\,dx = F(b) - F(a) \,, \tag{B.3}$$

and

$$\begin{aligned} F(x)\big|_j^{j+1} = {} & \frac{x^4\left(y''_j - y''_{j+1}\right)}{24x_j - 24x_{j+1}} + \frac{x^3\left(x_j y''_{j+1} - x_{j+1}y''_j\right)}{6x_j - 6x_{j+1}} \\ & + \frac{x^2\left(-x_j^2 y''_j - 2x_j^2 y''_{j+1} + 2x_j x_{j+1} y''_j - 2x_j x_{j+1} y''_{j+1} + 2x_{j+1}^2 y''_j + x_{j+1}^2 y''_{j+1} + 6y_j - 6y_{j+1}\right)}{12x_j - 12x_{j+1}} \\ & + \frac{x\left(x_j^2 x_{j+1} y''_j + 2x_j^2 x_{j+1} y''_{j+1} - 2x_j x_{j+1}^2 y''_j - x_j x_{j+1}^2 y''_{j+1} + 6x_j y_{j+1} - 6x_{j+1} y_j\right)}{6x_j - 6x_{j+1}} \,. \end{aligned} \tag{B.4}$$

B.2 TRAPEZOID INTEGRATION ON LOG-LOG SCALE

The trapezoidal rule is

$$\int_a^b f(x)\,dx = \frac{1}{2}(b-a)(f(b) + f(a)) \tag{B.5}$$

On a log-log scale, we have data $(\log x, \log f(x))$. If we want to integrate $f(x)$ on this scale, we need to change variables:

$$u = \log x \,, \qquad x = e^u \,, \tag{B.6}$$

$$g = \log f(x) \,, \quad f = e^g \,. \tag{B.7}$$

Then,

$$du = \frac{1}{x} dx \,, \tag{B.8}$$

giving

$$\begin{aligned} dx &= x du \\ &= e^u du \,. \end{aligned} \tag{B.9}$$

Now we have

$$\int_a^b f(x)\,dx = \int_{\log a}^{\log b} e^g e^u\,du = \int_{\log a}^{\log b} e^{(g+u)}\,du\,. \tag{B.10}$$

The trapezoidal rule for this integration is thus:

$$\frac{1}{2}(\log b - \log a)(e^{(\log f(b)+\log b)} + e^{(\log f(a)+\log a)}) = \frac{1}{2}(\log b - \log a)(bf(b) + af(a))\,. \tag{B.11}$$